



CHORUS

This is the accepted manuscript made available via CHORUS. The article has been published as:

Manipulating femtosecond spin-orbit torques with laser pulse sequences to control magnetic memory states and ringing

P. C. Lingos, J. Wang, and I. E. Perakis

Phys. Rev. B **91**, 195203 — Published 19 May 2015

DOI: [10.1103/PhysRevB.91.195203](https://doi.org/10.1103/PhysRevB.91.195203)

Manipulating Femtosecond Spin–Orbit Torques with Laser Pulse Sequences to Control Magnetic Memory States and Ringing

P. C. Lingos¹, J. Wang³, and I. E. Perakis^{1,2}

¹*Department of Physics, University of Crete, Box 2208, Heraklion, Crete, 71003, Greece*

²*Institute of Electronic Structure & Laser, Foundation for Research and Technology-Hellas, Heraklion, Crete, 71110, Greece and*

³*Ames Laboratory and Department of Physics and Astronomy, Iowa State University, Ames, Iowa 50010, USA*

(Dated: April 27, 2015)

Femtosecond (fs) coherent control of collective order parameters is important for non-equilibrium phase dynamics in correlated materials. Here we propose such control of ferromagnetic order based on using non-adiabatic optical manipulation of electron–hole (e – h) photoexcitations to create fs carrier–spin–pulses with controllable direction and time profile. These spin–pulses arise due to time–reversal symmetry breaking arising from non-perturbative spin–orbit and magnetic exchange couplings of coherent photocarriers. By tuning the non-thermal populations of exchange–split, spin–orbit–coupled semiconductor band states, we can excite *fs spin–orbit torques* that control complex magnetization pathways between multiple magnetic memory states. We calculate the laser–induced fs magnetic anisotropy in the time domain by using density matrix equations of motion rather than the quasi-equilibrium free energy. By comparing to pump–probe experiments, we identify a “sudden” out-of-plane magnetization canting displaying fs magnetic hysteresis which agrees with switchings measured by the static Hall magnetoresistivity. This fs transverse spin–canting switches direction with magnetic state and laser frequency, which distinguishes it from the longitudinal nonlinear optical and demagnetization effects. We propose that sequences of clockwise or counter-clockwise fs spin–orbit torques, photoexcited by shaping two-color laser–pulse sequences analogous to multi-dimensional Nuclear Magnetic Resonance (NMR) spectroscopy, can be used to timely suppress or enhance magnetic ringing and switching rotation in magnetic memories.

PACS numbers: 78.47.J-, 75.50.Pp, 75.30.Hx, 75.78.Jp

I. INTRODUCTION

Femtosecond (fs) control of switching between condensed matter states^{1–4} may address challenges posed by multi-functional devices used for information storage and processing on a single chip at up-to-thousand-times faster terahertz speeds. One of the main obstacles for widespread use of magnetic materials in such applications is the lack of efficient control of magnetization. Fast spin manipulation is one of the main challenges for spin-electronics, spin-photonics, magnetic storage, and quantum computation.⁵ To meet this challenge, different magnetic systems must be explored. In diverse systems ranging from ferromagnetic semiconductors^{6–8} to doped topological insulators,^{9,10} magnetic effects arise from exchange interactions ($\propto \mathbf{S} \cdot \mathbf{s}$) between two distinct sub-systems: mobile, spin–orbit–coupled electron spins (\mathbf{s}) and magnetic local moments (\mathbf{S}).¹¹ These interactions couple, for example, magnetic impurity spins with Dirac fermions in topological insulators⁹ or valence-band holes in (III,Mn)V semiconductors.⁶ Such couplings break time–reversal symmetry and result in ferromagnetic states with two distinct but strongly-coupled collective-spin order parameter components.^{6,9} When brought out of thermodynamic equilibrium, interacting mobile and local collective spins allow more “knobs” for manipulating ultrafast magnetism¹² by using fs laser pulses.

As is known in both semiconductors^{13–17} and metals,^{18–20} depending on the timescale, a distinction must be made between e – h quantum excitations, non-

thermal e and h populations, and Fermi–Dirac populations (see the schematic in Fig. 1(a)). Initially, only coherent e – h pairs are photoexcited (left part of Fig. 1(a)), which dephase within a time-interval T_2 . For T_2 shorter than the laser pulse duration, this e – h coherence is only important for determining the photoexcited e and h populations. The contribution of such non-thermal (i.e. non-Fermi–Dirac) carrier populations to the spin and charge dynamics must be taken into account when their relaxation times T_1 are not too short compared to the ~ 100 fs timescales of interest.¹⁸ Non-thermal population effects are observable in semiconductors^{13,14} and metals.^{18–20} Recent pump–probe measurements²¹ also identified a fs non-thermal hole spin relaxation in (Ga,Mn)As ferromagnetic semiconductors. This temporal regime lasts for 160–200 fs and diminishes with increasing temperature, together with the ferromagnetic order. It precedes a picosecond (ps) hole energy relaxation, which occurs on a time-scale of 1–2 ps and is not very sensitive to temperature. The above experimental observations²¹ indicate that the photohole populations redistribute between band states with different spin polarizations during $T_1 \sim 100$ fs prior to relaxation into hot Fermi–Dirac distributions (Fig. 1(a)).

While the quantum kinetics of charge photoexcitations has been studied,^{13,18} fs non-adiabatic magnetic correlation is not well-understood.^{1,3,4,22} Collective spin dynamics is triggered when coupled magnetic order parameter components are “suddenly” brought out of equilibrium via laser excitation. The relative contributions of coherent, non-thermal, and hot-Fermi–Dirac carrier

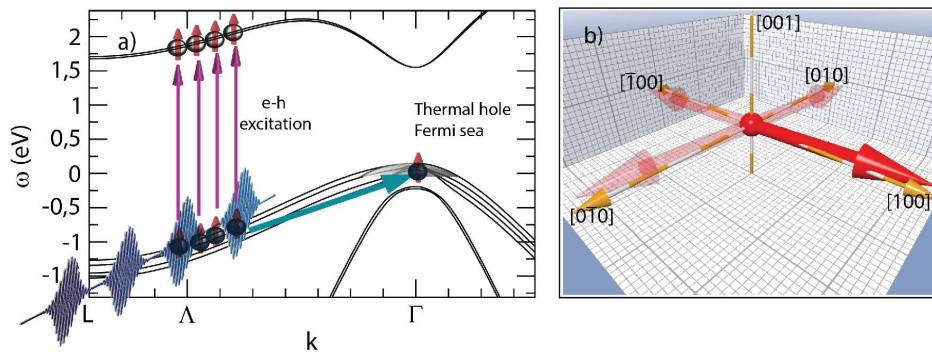


FIG. 1: (Color online) (a): Schematic of two contributions to the transient magnetic anisotropy: e - h excitations (non-thermal and coherent carrier contribution, left part) and Fermi sea holes (thermal contribution, right part). For $\hbar\omega_p \sim 3.1\text{eV}$, the holes are excited in high- k , non-parabolic, HH or LH exchange-split valence band states. (b): The thermal hole Fermi sea free energy gives four in-plane magnetic memory states X^+ , Y^+ , X^- , and Y^- , slightly tilted from the corresponding crystallographic axes.

spins interacting with local magnetic moments^{1,3,4} depend on laser intensity and frequency, relaxation parameters, material properties, and probed timescales. Sequences of fs laser-pulses analogous to multidimensional NMR spectroscopy^{15,23,24} offer possibilities for clarifying and controlling such transient magnetic responses. Here we show that coherent optical control of non-equilibrium mobile carrier spin induced by laser excitation of a non-thermal population imbalance can be used to suppress or start magnetization ringing and switching rotation by exerting *fs spin-orbit torque* sequences in controlled directions. We propose that such a non-adiabatic optical approach may allow control of magnetic states without relying on magnetic field pulses, circularly-polarized light,^{17,25,26} demagnetization,^{8,27-29} quasi-thermal processes,^{2,30-33} or the precession phase.³⁴

The fs photoexcitation of (Ga,Mn)As has revealed different transient magneto-optical responses, such as ultrafast increase (decrease) of magnetization amplitude under weak (strong) excitation^{8,28,29,35} and magnetization re-orientation due to spin-torque^{17,26} and spin-orbit torque.^{3,36,37} There is mounting evidence that non-thermal magnetic processes play an important role in the fs magnetization time evolution.^{3,17,36,37} (III,Mn)V heterostructures are advantageous for optical control of magnetic order due to their well-characterized optical and electronic properties and their manipulable carrier-induced ferromagnetism. Useful for demonstrating our theoretical predictions is that these systems have four different in-plane magnetic states (X^+ , Y^+ , X^- , and Y^-), due to bi-axial magnetic anisotropy between the [100] and [010] crystallographic axes (Fig. 1(b) and Appendix A). While in conventional ferromagnets switching involves spin-flipping between two magnetic states (spin-up/spin-down, uniaxial magnetic anisotropy), the existence of four magnetic states allows for complex multi-state switching pathways and more elaborate magnetization control schemes. Four-state magnetic memories may be useful for ultra-high-density magnetic record-

ing applications, as the two equivalent easy axes double the recording density by recording two bits of information on the same spot.³⁸ To take advantage of such multi-state magnetic memories for ultrafast spintronics applications, we must be able to selectively access all magnetic states in any desired sequence. There is no generally accepted scheme on how to do this. Optical spin manipulation has, however, reached a high level of sophistication^{3,8,17,25,33,34,36,38-42} and control of magnetization on a 100ps timescale has been demonstrated in various systems, by using magnetic field or laser-generated magnetic pulses⁴³⁻⁴⁵ or photoinduced effects.^{2,46} Two outstanding challenges must, nevertheless, be better addressed: (i) how to initiate and stop controlled deterministic switchings during fs time intervals, (ii) how to suppress the magnetic ringing associated with switchings, which limits the prospects for high-speed applications.⁴⁷ Such challenges also apply to conventional uniaxial magnetic memories. From a more general perspective, the non-thermal dynamical disentanglement, during coherent nonlinear optical excitation, of degrees of freedom that are strong-coupled in equilibrium, such as the mobile photocarrier and localized collective spins here, may lead to a better understanding of correlated systems.^{1,4,48,49} The advantage of using spin-charge quantum kinetics to overcome the limitations of incoherent processes for meeting the above challenges is now beginning to be recognized.^{1,3,4,17,41,42,50,51}

This work contributes to the debate of how fs coherent photoexcitation could drive and control ultrafast switchings^{1,12} and magnetic ringing.⁴⁷ We consider the very early non-thermal and coherent temporal regimes and focus mostly on magnetization changes that occur *during the fs laser pulse* and are triggered by the photoexcited carriers. We show that, by choosing appropriate sequences of time-delayed laser pulses, we can control the direction, magnitude, and time-profile of the short-lived non-thermal photocarrier spin. The latter drives the magnetization away from equilibrium by exerting fs spin-

orbit torque on the collective local spin. By coherent manipulation of the e - h photoexcitations, we photogenerate a controlled population imbalance between spin-orbit-coupled/exchange-split bands. Such photoexcited band carrier population and spin imbalance is not restricted by the chemical potential or temperature and leads to a controllable “sudden” magnetization canting in selected directions at desirable times. Based on direct manipulation of the above non-thermal processes by the optical field, we propose possible protocols that drive complex 360° magnetization pathways, here involving sequential 90° deterministic switchings between four different magnetic memory states. Such spin control, as well as suppression of both magnetic ringing and switching rotations, are possible without circularly-polarized light due to relativistic spin-orbit coupling of the photocarriers leading to spin-orbit torque.

For linearly-polarized fs optical pulses, we show that the photoexcited carrier spin direction and amplitude is determined by the competition between spin-orbit coupling, with characteristic energy $\Delta_{so} \sim 340 \text{ meV}$ given by the Γ -point energy splitting of the GaAs spin-orbit-split valence band, and the $\mathbf{S} \cdot \mathbf{s}$ magnetic exchange coupling, with characteristic energy $\Delta_{pd} = \beta c S \sim 100 \text{ meV}$ in Ga(Mn)As,⁶ where S and c denote the Mn spin amplitude and concentration respectively and β is the magnetic exchange constant. The time-reversal symmetry breaking can be characterized by the energy ratio Δ_{pd}/Δ_{so} ($\sim 1/3$ in (Ga,Mn)As). It leads to fs photoexcitation of short-lived mobile spin-pulses (\mathbf{s}), whose direction is controlled by selectively populating the continua of exchange-split heavy-hole (HH) or light-hole (LH) spin-orbit-coupled band states with different spin superpositions. We model the fs nonlinear photoexcitation processes, driven by sequences of time-delayed laser-pulse-trains, with density matrix equations-of-motion,¹³ which describe photocarrier populations coupled non-perturbatively to inter-band coherences and time-dependent local spins. Our time-domain calculations describe a non-equilibrium magnetic anisotropy during the laser pulse, which we estimate by treating strong band non-parabolicity and spin-orbit couplings using the tight-binding bandstructure of GaAs with mean-field magnetic exchange interaction.^{6,52} We relate the calculated photoexcitation of fs spin-orbit torque to existing experiments and make predictions for new ones to observe switchings by using pulse-shaping.

The paper is organized as follows. In Section II we discuss the symmetry-breaking processes leading to photoexcitation of a 100fs mobile carrier spin-pulse with direction and magnitude that depend on the ratio Δ_{pd}/Δ_{so} . In Section III we compare theory and experiment to demonstrate coherent control of fs spin-orbit torque direction and magnitude by tuning populations of four exchange-split HH and LH valence bands excited by a 100fs laser pulse. We show that the canting direction of the excited transverse (out-of-plane) fs magnetization component displays a magnetic hysteresis absent with-

out pump. In experiment, the above fs spin-canting can be distinguished from longitudinal amplitude and nonlinear optical effects by sweeping a perpendicular magnetic field. In Section IV we show that we can initiate controlled switching rotations to any one of the available magnetic states by shaping a laser-pulse train. In Section V we propose two protocols for controlling four sequential 90° switchings in clockwise or counter-clockwise directions. In Section VI we use two time-delayed laser-pulse-trains to suppress or enhance the nonlinear switching rotation at any intermediate state and to suppress magnetic ringing at any time, long or short. Rather than relying on the magnetization precession phase, we achieve this coherent control by switching the directions of fs spin-orbit torques. We end with conclusions and a broader outlook. In two Appendices we present the density matrix equations describing nonlinear coherent excitation of fs spin-orbit torque, distinguish the non-adiabatic/non-thermal from the adiabatic/thermal transient magnetic anisotropy, and treat the non-parabolic and anisotropic spin-orbit-coupled band continua.

II. FEMTOSECOND SPIN PHOTOEXCITATION

In this section we discuss the processes leading to photoexcitation of carrier spin with direction determined by non-perturbative symmetry-breaking interactions. In the systems of interest, the magnetic effects arise from antiferromagnetic interactions between localized and mobile (delocalized) carrier spins.⁶ In contrast to magnetic insulators studied before,²⁵ the localized electrons do not contribute to the fs magnetic anisotropy but mainly determine the magnetization (collective local spin)

$$\mathbf{S} = \frac{1}{cV} \sum_i \langle \hat{\mathbf{S}}_i \rangle, \quad (1)$$

where V is the volume and \mathbf{S}_i are the local magnetic moments at positions i , with concentration c . For example, in (III,Mn)V magnetic semiconductors, the local magnetic moments are pure $S=5/2$ Mn spins with zero angular momentum, $L=0$, and no spin-orbit interaction. The magnetic anisotropy comes from band electrons, which are clearly distinguished from the local spins. Unlike for the localized electrons, these band electrons are subject to spin-orbit interactions and couple directly to light. The spin-exchange coupling of such photoexcited mobile carriers with the local spins induces the magnetization dynamics of interest here. The widely-used mean-field treatment of the magnetic exchange interaction (Zener model) captures the symmetry-breaking of interest here.⁶ We thus consider the dynamics of a single-domain macrospin $\mathbf{S}(t)$ and neglect spatial fluctuations.^{40,41} This approximation describes metallic-like (III,Mn)V magnetic semiconductors.⁶

Our main goal here is to control the non-equilibrium spin of band carriers in order to manipulate the magnetization motion during fs timescales. While spin-lattice

coupling also affects the easy axis, lattice heating occurs on longer (ps) timescales, following energy transfer from the electronic system^{33,37} Unlike previous demagnetization studies, the optical control scheme proposed here does not rely on population changes due to laser-induced electronic heating.^{8,28,29} It is based on direct carrier-spin photoexcitation without circularly-polarized light. The laser excites e - h pairs between different exchange-split valence and conduction bands (Fig. 1(a)). The magnetic exchange interaction of interest mainly involves the photoexcited valence hole collective spin $\Delta\mathbf{s}_h(t)$. Denoting by $\mathbf{s}_{\mathbf{k}n}^h$ the contribution from valence band n and momentum \mathbf{k} , we obtain the total hole spin

$$\mathbf{s}_h(t) = \frac{1}{V} \sum_{\mathbf{k}} \sum_n \mathbf{s}_{\mathbf{k}n}^h(t). \quad (2)$$

Below we demonstrate coherent control of $\mathbf{s}_{\mathbf{k}n}^h(t)$ by exciting a non-thermal imbalance between different band states (n, \mathbf{k}) during the laser pulse. We describe this non-thermal population imbalance by extending the discrete- \mathbf{k} calculation of fs spin-orbit-torque in Ref. [3] to include the anisotropic continua of the non-parabolic (Ga,Mn)As bands. This allows us to estimate the photocarrier density and net spin of different bands as function of laser-pulse frequency and intensity for comparison to experiment. In addition, here we consider sequences of time-delayed laser-pulse-trains. The mechanism of Ref. [3] is analogous to the current-induced spin-orbit torque⁵³ observed in (Ga,Mn)As⁵⁴ and other spin-orbit-coupled ferromagnets. Unlike our earlier work¹⁷ on fs spin-transfer torque analogous to the one induced by spin-polarized currents in spintronics applications,^{55,56} which requires circularly-polarized light,²⁶ here spin is not conserved due to spin-orbit coupling. As a result, transfer of angular momentum from the photons is not necessary for carrier spin excitation. Instead, the photoexcited spin is determined by symmetry-breaking due to the competition between spin-orbit and magnetic exchange couplings.

To initiate ultrafast spin dynamics, we create a short-lived spin imbalance by optically controlling $\mathbf{s}_{\mathbf{k}n}^h(t)$ from different bands n and Brillouin zone (BZ) directions \mathbf{k} . For this we express the carrier spin in terms of the density matrix $\langle \hat{h}_{-\mathbf{k}n}^\dagger \hat{h}_{-\mathbf{k}n'} \rangle$ defined in terms of an adiabatic basis of band eigenstates created by the operators $\hat{h}_{-\mathbf{k}n}^\dagger$:

$$\mathbf{s}_{\mathbf{k}n}^h = \hat{\mathbf{s}}_{\mathbf{k}nn}^h \langle \hat{h}_{-\mathbf{k}n}^\dagger \hat{h}_{-\mathbf{k}n} \rangle + \sum_{n' \neq n} \hat{\mathbf{s}}_{\mathbf{k}nn'}^h \langle \hat{h}_{-\mathbf{k}n}^\dagger \hat{h}_{-\mathbf{k}n'} \rangle, \quad (3)$$

where $\hat{\mathbf{s}}_{\mathbf{k}n'n}^h$ are the spin matrix elements. The latter describes the direction of the carrier spin for the band state (n, \mathbf{k}). Such spin dependence is determined by spin-mixing due to the non-perturbative interplay of spin-orbit and magnetic exchange couplings, which is characterized by the energy ratio Δ_{pd}/Δ_{so} . The first term on the right hand side (rhs) of Eq. (3) describes the population contribution (coherent, non-thermal, and quasi-thermal transient populations). The second term describes a contribution due to coupling of different bands

(inter-valence-band coherence). The latter Raman coherence arises when spin is not conserved, $\hat{\mathbf{s}}_{\mathbf{k}nn'}^h \neq 0$, and vanishes in equilibrium. We choose as basis $\hat{h}_{-\mathbf{k}n}^\dagger$ the eigenstates of the adiabatic Hamiltonian (Appendix A)

$$H_b(\mathbf{S}) = H_0 + H_{so} + H_{pd}(\mathbf{S}_0). \quad (4)$$

$H_0 + H_{so}$ describes the bandstructure of the parent material (undoped GaAs here), due to the periodic lattice potential (H_0) and the spin-orbit coupling (H_{so}).⁵² The symmetry-breaking is induced by the magnetic exchange interaction $H_{pd}(\mathbf{S}_0)$, Eq.(A1).⁶ Here, \mathbf{S}_0 denotes the slowly-varying contribution to the local macrospin that switches or oscillates during ps timescales (adiabatic contribution). The valence hole and conduction electron basis states, $\hat{h}_{-\mathbf{k}n}^\dagger$ and $\hat{e}_{\mathbf{k}m}^\dagger$ respectively, were obtained by diagonalizing $H_b(\mathbf{S}_0)$ using the tight-binding approximation of Ref. [52] (Appendix A).

In (III,Mn)V semiconductors, a thermal hole Fermi sea bath, characterized by the Fermi-Dirac distribution $f_{n\mathbf{k}}$, is already present in the ground state (Fig. 1(a)).⁶ Similar to ultrafast studies of the electron gas in metals¹⁸ and semiconductors,⁵⁷⁻⁵⁹ we distinguish this quasi-equilibrium contribution to Eq.(3) from the non-Fermi-Dirac femtosecond contribution (Appendix A):

$$\langle \hat{h}_{\mathbf{k}n}^\dagger \hat{h}_{\mathbf{k}n'} \rangle = \delta_{nn'} f_{n\mathbf{k}} + \Delta \langle \hat{h}_{\mathbf{k}n}^\dagger \hat{h}_{\mathbf{k}n'} \rangle. \quad (5)$$

At quasi-equilibrium, only the Fermi-Dirac populations contribute. These are characterized by a temperature and chemical potential and give the adiabatic field^{6,25,37}

$$\gamma \mathbf{H}_{FS}[\mathbf{S}] = -\frac{\partial E_h(\mathbf{S})}{\partial \mathbf{S}}, \quad (6)$$

where γ is the gyromagnetic ratio and

$$E_h(\mathbf{S}) = \sum_{\mathbf{k}n} \varepsilon_{n\mathbf{k}}^v f_{n\mathbf{k}} \quad (7)$$

is the total (free) energy of the relaxed Fermi-Dirac carriers. The latter defines the magnetic memory states of Fig.1(b) (Appendix A). $\varepsilon_{n\mathbf{k}}^v(\mathbf{S})$ are the (valence band) eigenvalues of the adiabatic Hamiltonian H_b for frozen local spin \mathbf{S} . The laser-induced heating of the Fermi-Dirac hole distribution ($f_{n\mathbf{k}}$) is one source of demagnetization,^{28,29} while the subsequent heating of the lattice is also known to thermally alter the magnetic anisotropy fields during ps timescales.^{32,33} Since the changes of this electronic E_h with \mathbf{S} are notoriously small for numerical calculations of the quasi-equilibrium magnetic anisotropy,^{37,60} while the low-energy states of (III,Mn)V systems are complicated by sample-dependent disorder, impurity bands, defect states, and strain,^{6,28,39,61} here we approximate $E_h(\mathbf{S})$ by using the symmetry-based Eq.(A9) with parameters extracted from experiment.^{6,39,61} In this way, we introduce the realistic four-state magnetic memory of the (III,Mn)V materials. For the low 10-100 μ J/cm²

pump fluences considered here, we neglect the laser-induced changes in the Fermi–Dirac distribution temperature and chemical potential, which add to the predicted effects on the timescale of energy and population relaxation.²¹ Calculations assuming Fermi–Dirac distributions^{28,37} gave order-of-magnitude smaller magnetization dynamics than experiment and concluded that the non-equilibrium hole distribution must be very broad.²⁸ Here we study the possible role of short-lived non-Fermi–Dirac populations, which are observed prior to full electronic thermalization²¹ (we assume $T_1 \sim 100$ fs). We calculate the fs anisotropy due to such non-thermal spin populations in the time domain, by solving the mean-field equations of motion for $\Delta(\hat{h}_{\mathbf{k}n}^\dagger \hat{h}_{\mathbf{k}n'})$ derived with time-dependent Hamiltonian (Appendix A)

$$H(t) = H_b(\mathbf{S}_0) + \Delta H_{exch}(t) + H_L(t). \quad (8)$$

While the adiabatic $H_b(\mathbf{S}_0)$ changes during 10's of ps, the other two contributions to Eq.(8) are non-adiabatic and vary during fs timescales. $H_L(t)$, Eq. (A3), describes the dipole coupling of the fs laser E -field,¹³ while

$$\Delta H_{exch}(t) = \frac{1}{V} \sum_{\mathbf{k}} \beta_{\mathbf{k}} c \Delta \mathbf{S}(t) \cdot \hat{s}_{\mathbf{k}}^h, \quad (9)$$

where $\hat{s}_{\mathbf{k}}^h$ is the hole spin operator and

$$\Delta \mathbf{S}(t) = \mathbf{S}(t) - \mathbf{S}_0, \quad (10)$$

describes the ‘‘sudden’’ changes in magnetization during the fs photoexcitation. We assume exchange constant $\beta_{\mathbf{k}} \approx \beta$ for the relevant range of \mathbf{k} .

We describe the non-Fermi–Dirac electronic contribution $\Delta(\hat{h}_{\mathbf{k}n}^\dagger \hat{h}_{\mathbf{k}n'})$, Eq.(5), similar to the well-established Semiconductor Bloch Equation^{13,62} or local-field^{16,63} Hartree–Fock treatments of ultrafast nonlinear optical response. In particular, we solve coupled equations of motion for the electronic populations and inter-band coherences $\langle \hat{h}_{\mathbf{k}m}^\dagger \hat{h}_{\mathbf{k}n} \rangle$, $\langle \hat{e}_{\mathbf{k}m}^\dagger \hat{e}_{\mathbf{k}n} \rangle$, and $\langle \hat{e}_{\mathbf{k}m}^\dagger \hat{h}_{-\mathbf{k}n} \rangle$, which are non-perturbatively coupled to the time-dependent local spin $\mathbf{S}(t)$. This coupling modifies the electronic dynamics, which, in turn, modifies the motion of $\mathbf{S}(t)$ (Appendix A). To obtain meaningful numerical results in the case of switching, the basis defined by the adiabatic $H_b(\mathbf{S}_0)$ is constantly adjusted due to the large changes in \mathbf{S}_0 during the time-evolution. Our equations of motion describe, in addition, the non-adiabatic effects of $\Delta \mathbf{S}(t)$ on the time-dependent band states. We consider linearly-polarized optical pulses with zero angular momentum. We do not include the carrier-carrier, carrier-phonon, and carrier-impurity interactions in the Hamiltonian, but treat the photocarrier relaxation phenomenologically, by introducing e - h dephasing times T_2 and non-thermal population relaxation times T_1 . Our calculation thus describes the ‘‘initial condition’’ that brings the system out of equilibrium and initiates relaxation.^{28,51} The latter redistributes the non-thermal carriers among band states with different spins and momentum directions \mathbf{k} , which leads to

spin relaxation. Here we model this by introducing the relaxation time T_1 of the populations $\langle \hat{h}_{-\mathbf{k}n}^\dagger \hat{h}_{-\mathbf{k}n} \rangle$ determining the hole spin in Eq.(3), which reflects the 100–200fs hole spin relaxation time measured experimentally in (Ga,Mn)As.²¹ The latter was calculated in Ref. [51] to be several 10's of fs. On the other hand, momentum scattering and carrier relaxation give T_2 's of few 10's of fs.^{6,51} Below we estimate the dependence of the predicted non-thermal effects on T_1 and T_2 .

The calculations in this paper describe photogeneration of spin that initiates fs dynamics. We describe the average hole spin $\Delta \mathbf{s}_h(t)$ of e - h pairs excited in band continuum states determined by the pump laser frequency ω_p . The main results were obtained for $\hbar\omega_p \approx 3.1$ eV.^{7,36} For such pump frequencies, the (Ga,Mn)As disorder-induced impurity/defect states²⁸ do not contribute significantly and the photoexcited carriers are initially well-separated in energy from the Fermi sea holes (see Fig. 1(a)). We mainly excite HH and LH band states along the eight $\{111\}$ symmetry lines of the BZ, at high \mathbf{k} , where the conduction and valence bands are strongly non-parabolic and almost parallel to each other.⁷ As a result, a large number of inter-band optical transitions are excited simultaneously and a broad continuum of hole band momenta \mathbf{k} , inaccessible at quasi-equilibrium, is populated during the laser pulse (see Fig. 1(a)). Such highly anisotropic band continua are accounted for here as described in Appendix B. Magnetic anisotropy arises since, due to the symmetry-breaking introduced by $\mathbf{S}(t)$, the eight photoexcited $\{111\}$ directions are not equivalent. The calculated hole spin matrix elements $\hat{s}_{\mathbf{k}nn'}^h$, which determine the photohole spin direction, are fairly constant for each given band over a wide range of high \mathbf{k} . Optical transitions at $\hbar\omega_p \approx 3.1$ eV then add constructively to the hole spin from each of the $\{111\}$ directions and enhance its magnitude, which depends on the total photohole densities $\frac{1}{V} \sum_{\mathbf{k}} \Delta(\hat{h}_{-\mathbf{k}n}^\dagger \hat{h}_{-\mathbf{k}n})$ for each band n assuming smooth \mathbf{k} -dependence of the exchange constant $\beta_{\mathbf{k}}$. By tuning the pump around 3.1eV, timescalewe control a short-lived imbalance between the populations of bands with different spin-admixtures due to spin-orbit coupling. Our present calculations describe $\Delta \mathbf{s}_h(t)$ prior to inter-band relaxation or large momentum scattering between different \mathbf{k} -directions, which occur on a timescale T_1 of spin relaxation. On the other hand, pump frequencies $\hbar\omega_p \approx 1.5$ eV³⁷ excite smaller \mathbf{k} along $\{100\}$, $\{010\}$, $\{001\}$, $\{110\}$, $\{101\}$, $\{011\}$, and $\{111\}$ symmetry directions,⁶⁴ as well as impurity/defect states inside the semiconductor bandgap.^{6,28} Fig. 6 shows the quantitative differences between $\hbar\omega_p \approx 1.5$ eV and $\hbar\omega_p \approx 3.1$ eV, which arise from the differences in bandstructure. In addition to the difference in closely-lying valence bands, disorder-induced states, and density of states at different energies, the \mathbf{k} -dependence of the spin matrix elements $\hat{s}_{\mathbf{k}nn'}^h$ determining the photoexcited spin is stronger for the small wavevectors contributing around $\hbar\omega_p \approx 1.5$ eV.

Important for bringing the coupled local and mobile spin sub-systems away from equilibrium is their differ-

ent dynamics. For example, unlike for the band carriers, there is no spin-orbit or optical coupling of the local spins. In equilibrium, the local and mobile collective spins are correlated in the ferromagnetic state, so that $\mathbf{S} \times \mathbf{H}_{FS} = 0$.⁶ Within the mean-field approximation, $\mathbf{S}(t)$ is driven out of this equilibrium configuration by both quasi-equilibrium (\mathbf{H}_{FS}) and non-thermal ($\Delta\mathbf{s}_h$) carrier spins according to a Landau-Lifshitz-Gilbert equation:

$$\partial_t \mathbf{S} = -\gamma \mathbf{S} \times \mathbf{H}_{FS}[\mathbf{S}(t)] - \beta \mathbf{S} \times \Delta\mathbf{s}_h(t) + \frac{\alpha}{S} \mathbf{S} \times \partial_t \mathbf{S}, \quad (11)$$

where α characterizes the slow local spin precession damping.³³ The longitudinal magnetization amplitude changes, due to spin-charge correlations,^{4,28,40,41} are not captured by this mean-field approximation.

The dynamics of the mobile carrier spins depends, in addition to magnetic exchange interaction with the local spins, on spin-orbit coupling, direct nonlinear coupling to the optical field, and fast carrier relaxation:¹⁷

$$\partial_t \mathbf{s}_\mathbf{k}^h = \beta \mathbf{C} \mathbf{S} \times \mathbf{s}_\mathbf{k}^h + i \langle [H_{so}, \mathbf{s}_\mathbf{k}^h] \rangle + Im \mathbf{h}_\mathbf{k}(t) + \partial_t \mathbf{s}_\mathbf{k}^h|_{rel}. \quad (12)$$

The above equation is not useful here, as it does not distinguish between different bands in order to treat the spin-orbit coupling H_{so} . Nevertheless, it demonstrates four processes that determine the non-thermal carrier spin. The first term describes spin-torque due to magnetic exchange. The second term describes *spin-orbit torque*, obtained here by calculating the density matrix Eq.(5). The third term describes the Raman-type coherent nonlinear optical processes that excite the carrier spin.¹⁷

$$\mathbf{h}_\mathbf{k}(t) = 2 \sum_{mn} \langle \hat{h}_{-\mathbf{k}n} \hat{e}_{\mathbf{k}m} \rangle \sum_{m'} \mathbf{d}_{\mathbf{k}mm'}^*(t) \cdot \mathbf{s}_{\mathbf{k}m'n}^h, \quad (13)$$

where $d_{\mathbf{k}mm'} = \mu_{\mathbf{k}mm'} \cdot \mathbf{E}$ are the Rabi energies of optical transitions between band states ($m\mathbf{k}$) and ($m'\mathbf{k}$) and \mathbf{E} is the laser E -field. The last term describes spin relaxation.

The non-perturbative interplay between spin-orbit and magnetic exchange couplings determines the direction and magnitude of the net spin excited by a fs laser pulse. Fig. 2 shows a strong dependence of the maximum and direction of the photoexcited hole-spin-pulse $\beta\Delta\mathbf{s}_h(t)$ on the energy ratio Δ_{pd}/Δ_{so} . We obtained this result by solving the coupled equations of motion of Appendix A. In the ground state, the magnetization \mathbf{S}_0 points along the X^+ easy axis (Fig. 2). For $\Delta_{pd} \ll \Delta_{so}$, the net spin $\Delta\mathbf{s}_h$ is negligible without circularly-polarized light, since all symmetric directions in the BZ are excited equally. With increasing Δ_{pd} , the magnetic exchange interaction introduces a preferred direction along $\mathbf{S}(t)$. This breaks the time-reversal symmetry of GaAs and results in a net $\Delta\mathbf{s}_h(t)$ while the laser pulse couples to the magnetic system. With increasing Δ_{pd}/Δ_{so} , this $\Delta\mathbf{s}_h$ increases and its direction changes. For $\Delta_{pd}/\Delta_{so} \sim 1/3$ (as in (Ga,Mn)As), Fig. 2 shows that the in-plane component of the fs anisotropy field $\beta\Delta\mathbf{s}_h$ points close to the $[\bar{1}\bar{1}0]$ diagonal direction for

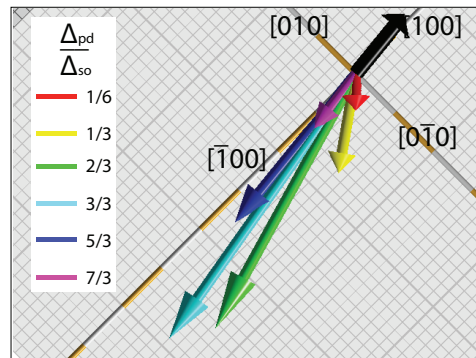


FIG. 2: (Color online) Maximum of anisotropy spin-pulse $\beta\Delta\mathbf{s}_h(t)$, photoexcited by a single 100fs linearly-polarized laser pulse, as function of the energy ratio Δ_{pd}/Δ_{so} that characterizes the time-reversal symmetry breaking. The direction of the ground-state magnetization is along the X^+ easy axis, shown by the black arrow close to $[100]$. $\hbar\omega_p = 3.14\text{eV}$, $E_0 = 7 \times 10^5 \text{V/cm}$, $T_1 = 100\text{fs}$, $T_2 = 50\text{fs}$.

$\hbar\omega_p = 3.14\text{eV}$. As discussed below, this result explains the experimental observations. The above $\Delta\mathbf{s}_h(t)$ only lasts during the 100fs laser pulse and drives a “sudden” magnetization canting $\Delta\mathbf{S}(t)$ via fs spin-orbit torque. As Δ_{pd} approaches Δ_{so} , $\Delta\mathbf{s}_h$ is maximized while it changes direction. The photohole spin decreases again for $\Delta_{pd} \gg \Delta_{so}$.

III. EXCITING f_s SPIN DYNAMICS WITH A SINGLE PULSE: THEORY VS EXPERIMENT

Ultrafast magneto-optical experiments in (III,Mn)V semiconductors have revealed control of magnon oscillations with frequency $\Omega \sim 100\text{ps}^{-1}$. In these experiments, the magnon excitation is suppressed (enhanced) with a laser pulse delayed by τ such that $\Omega\tau = \pi$ ($\Omega\tau = 2\pi$).³⁴ In this paper we propose a different optical control scheme, based on controlling the direction, duration, and magnitude of fs spin-orbit torque sequences photoexcited at any time τ . First, however, we validate our original prediction³ of fs spin-orbit torque as a source of non-thermal laser-induced spin dynamics in (III,Mn)V materials. For this we connect here numerical results obtained for anisotropic and non-parabolic band continua with the few existing experiments showing f_s spin dynamics. In this section we show that our calculations validate the experimental observation in Ref. [36] of fs magnetic hysteresis and spin rotations excited by a single 100fs laser pulse in (Ga,Mn)As. We also show that they are consistent with the observation of “sudden” non-thermal (sub-picosecond) magnetization rotation reported in Ref. [37]. The fs temporal regime of non-thermal spin dynamics, which is less understood as compared to the extended ps timescales, is most relevant for the main purposes of this paper, which are to (i) make numerical predictions of all-optical control of spin rotation and magnetic ring-

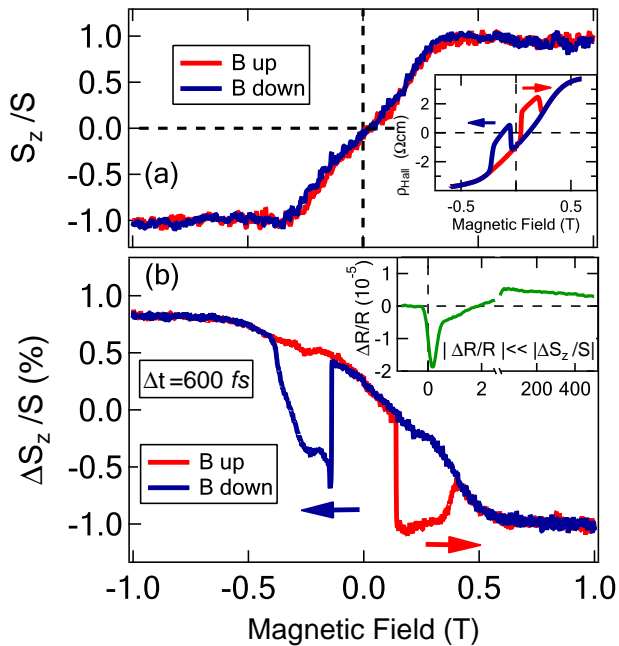


FIG. 3: (Color online) By sweeping a perpendicular B -field, tilted by 5° from the Z -axis and 33° from the X -axis, “up” (red curve) and “down” (blue curve), we measure the B -dependence of the magnetization component perpendicular to the sample plane at 5K in the polar MOKE geometry (normalized by the ~ 4 mrad MOKE angle). (a): Static measurements (no pump). The coinciding “up” and “down” polar Kerr rotation angles θ_K show no magnetic hysteresis in the static case. In contrast, the Hall magnetoresistivity (inset) shows 90° in-plane magnetization switchings between the XZ and YZ planes, which manifest themselves as a “major” hysteresis loop. This difference implies that the magneto-optical signal in the present configuration is insensitive to the in-plane magnetization components, which switch. (b): Time-dependent measurements (pump on). The pump-induced change $\Delta\theta_K/\theta_K \approx \Delta S_z/S$, measured at probe time delay $\Delta t = 600$ fs for the same experimental conditions as in (a), shows a magnetic hysteresis similar to the static Hall magnetoresistivity. In comparison, the ultrafast differential reflectivity $\Delta R/R$ (inset) is up to thousand times smaller, which points to a magnetic origin of our $\Delta\theta_K/\theta_K$ signal.

ing, and (ii) propose complex switching protocols similar to multidimensional NMR, but based on fs laser pulse trains with various timing sequences and colors.

We start by discussing the experimental technique and (Ga,Mn)As sample used in Ref. [36]. We argue that our static and time-resolved experimental curves and their comparison with our theory indicate that the measured fs magneto-optical response for in-plane ground state magnetization is dominated by the transverse out-of-plane magnetization component S_z and the polar Kerr effect. We performed *two-color* time-resolved MOKE spectroscopy in order to better discern the genuine spin dynamics.^{8,65} Prior to the relaxation time T_1 , the high-energy non-thermal carriers excited by the 3.1eV pump

have small effect on the population of the low-energy band states seen by the 1.55eV probe. By comparing two-color Kerr rotation, ellipticity, and reflectivity pump-probe signals, we distinguish fs magnetization dynamics from nonlinear optical effects^{65,66} and identify a fs component displaying magnetic hysteresis induced by a perpendicular magnetic field.

Different magneto-optical effects are observed for different experimental set-ups. These may be broadly divided based on rotation angles $\theta_K(\mathbf{S})$ of the linearly-polarized probe electric field that are linear (odd) or quadratic (even) functions of \mathbf{S} . Previous linear magneto-optical spectroscopy experiments in ferromagnetic (Ga,Mn)As observed a giant Magnetic Linear Dichroism (MLD) signal for probe frequencies between 1.4 and 2.4eV,^{67,68} with quadratic dependence on \mathbf{S} . In contrast, the polar Kerr effect signal⁶⁵ is linear in the perpendicular S_z , without contribution from the in-plane spin components. The relative contribution of these two magneto-optical effects depends on the direction of light propagation \mathbf{k} and linear polarization \mathbf{E} with respect to the magnetization.^{65,67,68} Below we discuss the details of our experimental design and measured quantities.

The main sample studied here was grown by low-temperature molecular beam epitaxy (MBE) and consists of a 73-nm $\text{Ga}_{0.925}\text{Mn}_{0.075}\text{As}$ layer on a 10nm GaAs buffer layer and a semi-insulating GaAs [100] substrate. The in-plane ground state magnetization points along the X^+ easy axis close to the [100] crystallographic axis (Fig. 1(b)). For probe we used a NIR beam tuned at 1.55 eV, which propagates along a direction almost perpendicular to the sample plane ($\sim 0.65^\circ$ from the normal). The probe linear polarization is along [100], almost *parallel* to the ground state magnetization. The pump, on the other hand, was chosen as a UV beam tuned at $\hbar\omega_p = 3.1$ eV and was linearly-polarized at an angle $\sim 12^\circ$ from [100], with $\sim 10\mu\text{J}/\text{cm}^2$ peak fluence smaller than in previous experiments. Its $\sim 40\text{nm}$ penetration depth implies photoexcitation of only the 73nm-thick magnetic layer. The duration of the pump and probe pulses was 100fs and 130fs respectively, while the laser repetition rate was 76 MHz. A detailed description of our measurement may be found in section 3.1.2 of Ref. [65]. We extracted the background-free MOKE rotation angle θ_K by measuring the difference between s- and p-polarized probe light (linear polarization along the [100] and [010] crystallographic axes, i.e. parallel and perpendicular to the ground state magnetization). This is achieved by reflecting s-polarized light from the sample surface and then passing it through a combination of a half wave plate and Wollaston prism. Further technical details of our setup can be found in Ref. [8]. The chosen design minimizes the MLD contribution to our measured magneto-optical signals shown in Figs. 3–4, discussed below. The sweeping of an external magnetic field B almost perpendicular to the sample and easy axes plane produced the fs magnetic hysteresis shown in Fig. 3(b). This laser-induced hysteresis is consistent with the behavior of the static Hall

magnetoresistance (inset of Fig. 3(a)), which is known to arise from in-plane magnetization switchings between the four easy axes of Fig. 1(b). However, no magnetic hysteresis is observed in the linear magneto-optical signal without pump for the same experimental conditions (compare Figs. 3(a) and 3(b)). This result implies that the measured signal is dominated by S_z (polar Kerr effect) for the linear polarization direction used here.

As discussed e.g. in Refs. [65,66], a signature of genuine magnetization dynamics is the complete overlap of the pump-induced transient Kerr rotation $\Delta\theta_K/\theta_K$ and ellipticity $\Delta\eta_K/\eta_K$ signals. Indeed, nonlinear optical effects are expected to contribute differently to $\Delta\theta_K$ and $\Delta\eta_K$, as determined by the real and imaginary parts of the pump-induced changes in the Fresnel coefficients.^{65,66} In our experiment, $\Delta\theta_K/\theta_K \approx \Delta\eta_K/\eta_K$ throughout the fs time-scan range of interest.³⁶ We thus conclude that the measured $\Delta\theta_K/\theta_K$ primarily reflects the pump-induced magnetization $\Delta S_z/S$. This claim is further supported by the simultaneous measurement of a differential reflectivity signal $\Delta R/R$ (inset, Fig. 2(b)) that is up to thousand times smaller than the Kerr rotation and ellipticity signals. The above two experimental observations imply that the relative pump-induced change in the Fresnel coefficients, which adds to the magneto-optical response,⁶⁵ is much smaller than $\Delta S_z/S$ in the studied configuration. As discussed below, the magnetic origin of the measured fs $\Delta\theta_K/\theta_K$ is further seen when sweeping an external B-field slightly tilted from the perpendicular direction (Fig.4(a)), which reveals a magnetic hysteresis absent in the measured linear response.

The interpretation of the static θ_K in the absence of pump (Fig. 3(a)) does not suffer from the complexity of interpreting the fs pump-probe signal. $\theta_K(B)$ switches sign with B-field and saturates for $|B| > 250\text{mT}$. It coincides between “up” and “down” sweeps (no magnetic hysteresis). In sharp contrast, for the same experimental conditions, the static Hall magneto-resistivity ρ_{Hall} shows in-plane magnetic switchings (planar Hall effect), which manifest themselves as jumps in the four-state magnetic memory hysteresis [inset of Fig.3]. Since the measured static magneto-optical signals show no signature of the above in-plane magnetization switchings between the XZ and YZ planes, they are dominated by the polar MOKE Kerr effect that is proportional to S_z and thus insensitive to the in-plane magnetization.^{65,67} In contrast, MLD⁶⁷ is a second-order effect and includes contributions such as $S_x S_y$ that are sensitive to the in-plane magnetization switching. Their absence in Fig. 3(a) implies that MLD is not the main origin of our measured magneto-optical signal, which thus is dominated by the polar Kerr effect and $S_z(B)$. Furthermore, the probe photon energy (1.55 eV) that we chose gives a MOKE angle of 4 mrad at 5K. This value is very close to the maximum MOKE angle quoted in the literature and few times larger than the typical MLD angles observed in (Ga,Mn)As samples. To understand why the polar Kerr effect dominates over MLD in our experimental set-

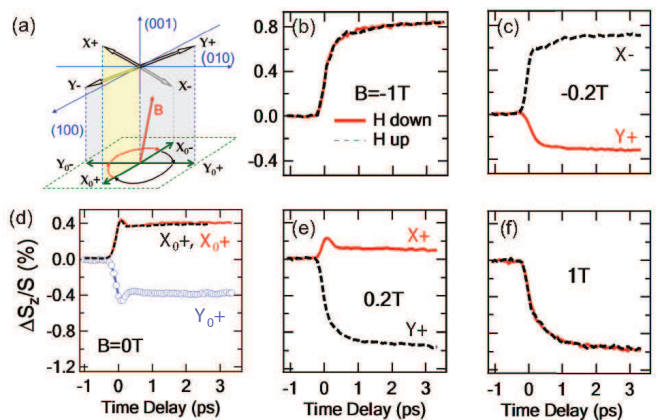


FIG. 4: (Color online) Magneto-optical pump-probe experimental measurements showing development of laser-induced magnetization canting $\Delta S_z(t)$ within $\sim 100\text{fs}$. This fs canting displays magnetic hysteresis and switches direction when switching in-plane magnetic state. (a) We sweep a perpendicular B-field, applied at a small angle $\sim 5^\circ$ from the [001] axis. This B-field tilts the $B=0$ in-plane easy axes (X_0^\pm and Y_0^\pm) out of the plane (Appendix A). (b)–(f): The “sudden” out-of-plane magnetization tilt $\Delta S_z/S$, induced by a 100fs laser pulse with fluence $\sim 7\mu\text{J}/\text{cm}^2$, switches direction when sweeping the B-field between $B=-1\text{T}$ and $B=1\text{T}$. The two sweeping directions correspond to increasing (“up”) and decreasing (“down”) B-field. For each of the measured $B=1\text{T}$, 0.2T , 0T , -0.2T , and -1T , the fs temporal profiles of $\Delta S_z/S$ depend on the equilibrium magnetic state switched by B.

up, we recall that two different geometries are used to measure magneto-optical signals: (i) probe linear polarization along [100], almost parallel to the ground state magnetization. This is the case here and, as discussed e.g. in Ref. [68], only minimal MLD is expected. (ii) the probe linear polarization is close to the [110] direction as in Ref. [68]. In this case, one measures a mixed signal with both MLD and polar MOKE contributions.⁶⁷ While MLD dominates in (Ga,Mn)As when the probe is polarized along the [110] or [1-10] directions,^{67,68} i.e. at $\sim 45^\circ$ degrees with respect to the easy axis, our data here was obtained for probe polarization along [100] or [010].

Unlike previous experiments that measured the dynamics of (III,Mn)V ferromagnets on a ps timescale, Fig. 4 shows directly the $\sim 100\text{fs}$ temporal profile of the pump-probe magneto-optical signal as function of perpendicular B-field. The pump optical field, with amplitude $E_0 \sim 2 \times 10^5 \text{V}/\text{cm}$ and fluence $\sim 7\mu\text{J}/\text{cm}^2$, excites a total photohole density of $n \sim 6 \times 10^{18} \text{cm}^{-3}$, a small perturbation of the $3 \times 10^{20} \text{cm}^{-3}$ ground state hole density in our (Ga,Mn)As sample. As seen in Fig. 3, our experimental set-up measures the transverse magnetization component $\Delta S_z(t)$, which is perpendicular to the ground state magnetization. During fs timescales, Fig. 4 shows a systematic B-field dependence and sign-switching of $\Delta\theta_K$ that is absent in θ_K without pump. This behavior correlates with the magnetic switchings observed in

the static transverse Hall magnetoresistivity and demonstrates that the pump-induced out-of-plane magnetization component $\Delta S_z(t)$ switches direction when the in-plane magnetic state switches. Furthermore, the step-like temporal profile of $\Delta\theta_K/\theta_K \approx \Delta S_z/S$ indicates that such spin re-orientation completes during the laser pulse and is therefore driven by $e-h$ photoexcitation. This fs time-dependence is clearly distinguished from subsequent magnon oscillations during ~ 100 ps times.²¹

We now relate our theory to the observed dependence of $\Delta\theta_K/\theta_K$ with ~ 100 fs duration on the transverse magnetic field B of Fig. 4(a). For $B=0$, the magnetic states X_0^\pm and Y_0^\pm lie inside the plane (Fig. 1(b)). For $B \neq 0$, Eq. (A11) gives an out-of-plane canting of X^\pm and Y^\pm easy axes (Fig. 4(a)). The measured smooth change of static Kerr rotation angle θ_K as function of B -field reflects such canting without magnetic hysteresis. As shown by our calculation below, while S_z varies smoothly with increasing or decreasing B -field, when the magnetization switches between X^\pm and Y^\pm the direction of pump-induced fs component ΔS_z reverses. The above dependence of pump-induced magnetization reversal on the easy axis cannot be explained by conventional non-linear optical effects or magnetization amplitude longitudinal changes.^{8,27-29} When the latter dominate, X^+ (X^-) give the *same* ΔS_z as Y^+ (Y^-), as the two in-plane magnetic states are equivalent (symmetric) with respect to the probe propagation direction perpendicular to the X-Y plane. Fig. 4(d) ($B=0$) and Figs. 4(c) and (e) ($B=\pm 0.2T$) clearly show that this is not the case in the experiment. In sharp contrast, for $B=\pm 1T$, Figs. 4(b) and (f) show the same fs changes for both increasing and decreasing B . The fs response is independent of the easy axis for large B , which aligns the magnetization along $[001]$. Our calculations show that the fs magnetization re-orientation due to fs spin-orbit torque diminishes with increasing perpendicular B , consistent with the above behavior.

For $B=0$, Fig. 4(d) reveals a *symmetric and opposite* out-of-plane fs canting $\Delta S_z(t)$ between the X_0 and Y_0 initial states. In this case, the initial magnetization \mathbf{S}_0 lies inside the sample plane (Fig. 4(a)) and thus the observed $\Delta S_z(t)$ cannot be associated with an amplitude change, as it occurs in a direction $[001]$ perpendicular to \mathbf{S}_0 . For large B , on the other hand, the magnetization aligns with the B -field along $[001]$, $S_z \approx S$, and thus $\Delta S_z(t)$ primarily reflects longitudinal fs changes in magnetization amplitude.^{28,41} When $S_z \approx 0$, as for $B=0$, $\Delta S_z(t)$ reflects transverse changes in magnetization direction. We conclude that the observation of opposite sign of laser-induced fs $\Delta S_z(t)$ between the X_0^\pm and Y_0^\pm states (Fig. 4(d)) can only arise from fs magnetization rotation towards opposite out-of-plane directions. Except for this sign difference, the fs temporal profiles of $\Delta S_z/S$ in Fig.4(d) are symmetric between X_0 and Y_0 . This symmetry implies that the out-of-plane ΔS_z is driven by a laser-induced anisotropy field pulse that points close to the diagonal direction between X_0 and Y_0 . The step-like

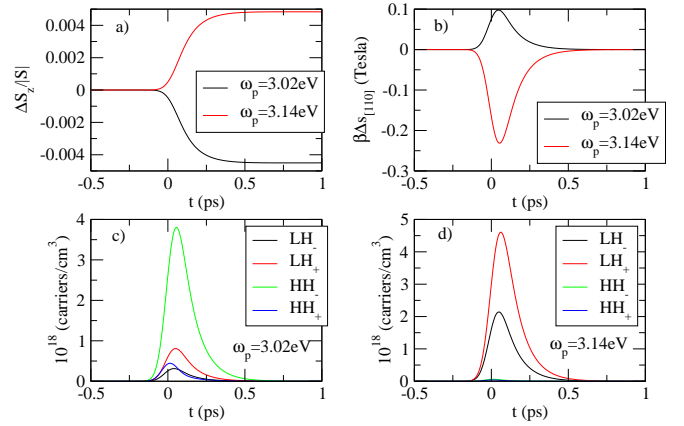


FIG. 5: (Color online) Frequency dependence of local and mobile spin dynamics and photohole populations following excitation by a 100fs linearly-polarized laser pulse with low pump fluence $\sim 10 \mu\text{J}/\text{cm}^2$, with initial magnetization along the X^+ easy axis. (a): Comparison of “sudden” out-of-plane magnetization for $\hbar\omega_p=3.14\text{eV}$ (LH optical transitions) and $\hbar\omega_p=3.02\text{eV}$ (HH optical transitions). (b): Comparison of non-adiabatic photoexcited hole spin component along $[110]$ for the two above frequencies. (c): Photoexcited non-thermal hole total populations of the four exchange-split HH and LH bands for $\hbar\omega_p=3.02\text{eV}$. (d): Same as (c) for $\hbar\omega_p=3.14\text{eV}$.

temporal profile implies that this field has ~ 100 fs duration. The above experimental observations are consistent with the direction and duration of the calculated $\Delta\mathbf{s}_h$, shown in Fig. 2 for anisotropy parameter $\Delta_{pd}/\Delta_{so} \sim 1/3$ as in (Ga,Mn)As. Such carrier-spin-pulse, discussed further below, exerts a fs spin-torque $\propto \Delta\mathbf{s}_h \times \mathbf{S}_0$, whose out-of-plane direction changes sign for \mathbf{S}_0 along X_0 or Y_0 while its magnitude remains the same. Note here that, although laser-induced thermal effects due to spin-lattice coupling can also change the equilibrium easy axis, such changes occur gradually in time, over many ps.^{33,37} In contrast, here we observe step-like magnetization changes that follow the 100fs laser pulse and are consistent with our predicted fs spin-orbit torque. Note also that the experiment may show, in addition to the predicted magnetic contribution, “coherent artifacts” that appear e.g. as a small “overshoot” at the very beginning of Fig. 4(d). Such details do not change our conclusion about laser-induced spin-canting during the 100fs pulse.

To compare our theory to Fig. 4, we first consider $B=0$ and show in Fig. 5 the calculated spin and charge dynamics for a single linearly-polarized 100fs pump laser pulse with electric field amplitude $E_0=2 \times 10^5 \text{V}/\text{cm}$ similar to the experiment. We compare the spin and charge population dynamics for two different laser frequencies, $\hbar\omega_p=3.02\text{eV}$ and $\hbar\omega_p=3.14\text{eV}$, tuned to excite different HH and LH band continua. In Fig. 5(a) we show the development in time of the optically-induced out-of-plane local spin component $\Delta S_z(t)$. The calculated step-like fs temporal profile and magnitude for $T_1=100$ fs agrees with

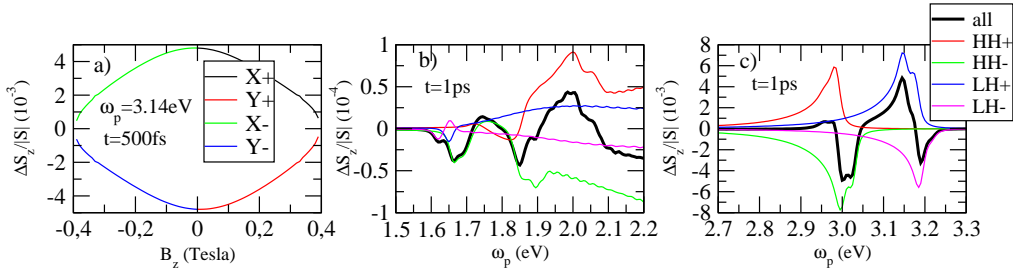


FIG. 6: (Color online) Calculated fs magnetic hysteresis and frequency dependence of the laser-induced magnetization canting $\Delta S_z/S$ due to fs spin-orbit torque. (a): The direction of out-of-plane component $\Delta S_z/S$ at $t=500$ fs depends on easy axis and magnetic field. This fs magnetic hysteresis diminishes with increasing perpendicular B -field, which suppresses laser-induced magnetization re-orientation, and separates “transverse” from “longitudinal” contributions to spin dynamics. (b) and (c): Frequency dependence of the laser-induced $\Delta S_z/S$ and its individual contributions from the four exchange-split HH and LH bands, calculated at $t=1$ ps for $E_0=2\times 10^5$ V/cm. We compare between $\hbar\omega_p\sim 1.5$ eV (b) and $\hbar\omega_p\sim 3$ eV (c). Spin-canting at the former frequency is smaller by factor of 10 due to the differences in bandstructure. The band continua significantly affect the frequency dependence of $\Delta S_z(t)$ as compared to discrete- \mathbf{k} special point calculations.

Fig. 4. Furthermore, we observe a reversal in the direction of ΔS_z when tuning the photoexcitation frequency. The fs spin-orbit torque leading to such $\Delta S_z(t)$ is exerted by the photohole spin-pulse $\Delta \mathbf{s}_h(t)$, whose component along the diagonal [110] direction is shown in Fig. 5(b) for the two above frequencies. The magnitude, direction, and temporal profile of both local and mobile spin components shown in Figs. 5(a) and (b) are consistent with the experimental results of Fig. 4(d). Important for controlling the four-state magnetic memory is that we are able to reverse the direction of the out-of-plane magnetization tilt ΔS_z , Fig. 5(a), and photoexcited hole spin-pulse, Fig. 5(b), by exciting e -HH ($\hbar\omega_p=3.02$ eV) or e -LH ($\hbar\omega_p=3.14$ eV) optical transitions. The origin of this spin-reversal can be seen by comparing the total populations $\frac{1}{V} \sum_{\mathbf{k}} \Delta(\hat{h}_{-\mathbf{k}n}^\dagger \hat{h}_{-\mathbf{k}n})$ for the four different exchange-split HH and LH valence bands n in all $\{111\}$ \mathbf{k} -directions. These band-resolved total populations are shown in Figs. 5(c) and (d) as function of time for $T_1=100$ fs, which is comparable to the measured²¹ and calculated⁵¹ hole spin relaxation time. More than one bands are populated simultaneously due to the energy dispersion and laser-pulse-width. With frequency tuning, we control a short-lived imbalance between these exchange-split bands with different spin-orbit couplings and spin admixtures. In this way, we coherently control the superposition of spin- \uparrow and spin- \downarrow states prior to spin relaxation, here mostly during the 100fs pulse.

The order of magnitude of the photocarrier densities calculated by including the band continua along all eight $\{111\}$ \mathbf{k} -directions using the GaAs tight-binding parameters of Ref. [52] (Appendix B) agrees with the experimentally-measured density, $n\sim 6\times 10^{18}/\text{cm}^3$, for the same pump fluence. For such photohole populations, we also obtain $\Delta S_z/S$ with the same order of magnitude and direction as in the experiment (compare Figs. 5(a) and 4(d)). The calculated ~ 250 mT component of $\beta\Delta \mathbf{s}_h(t)$ along [110], Fig. 5(b), agrees with the 100fs

magnetic anisotropy field extracted from Fig. 4(d) and is larger than typical fields obtained from calculations that assume a non-equilibrium Fermi-Dirac distribution.³⁷ This theory-experiment agreement indicates that non-thermal populations with lifetimes $T_1=100$ fs comparable to the hole spin lifetimes in (Ga,Mn)As^{21,51} can explain the observed impulsive $\Delta S_z(t)$.

Further evidence in support of our proposed fs spin-orbit torque mechanism is obtained from the pump-induced fs magnetic hysteresis observed in the experiment of Fig. 4. In Fig. 6(a) we compare the out-of-plane spin canting $\Delta S_z/S$ calculated at $t=500$ fs, as function of B -field pointing along the perpendicular [001] direction for the four B -dependent equilibrium magnetic states X^\pm and Y^\pm . Fig. 6(a) shows that switching between the X and Y initial magnetic states switches the sign of pump-induced $\Delta S_z(t)$ (fs magnetic hysteresis). Furthermore, Fig. 6(a) shows that fs magnetization re-orientation diminishes with increasing B . The above results are consistent with Fig. 4 and explain the observed coincidence of ΔS_z switchings with static planar Hall effect switchings,³⁶ as well as the absence of fs hysteresis at high B . While nonlinear effects such as dichroic bleaching also contribute to the fs magneto-optical signal, the observed systematic B -field dependence and magnetic hysteresis in the sign of $\Delta\theta_K/\theta_K$ indicate a non-adiabatic physical origin that is consistent with our calculations of fs spin-orbit torque.

For high B -fields, the magneto-optical signal comes only from longitudinal changes in the magnetization amplitude²⁹ and from nonlinear optical effects (Figs. 4(b) and 4(f)). The mean-field density matrix factorization used here does not capture magnetization amplitude changes, which appear at the level of electron-magnon spatial correlations.^{40,41} As discussed in Ref.[28], any photoinduced imbalance of spin- \uparrow and spin- \downarrow states will lead to fs demagnetization and inverse Overhauser effect, which however is independent of easy axis direc-

tion. While such imbalance may arise from photoinduced changes in the Fermi–Dirac temperature and chemical potential, a large electronic temperature increase is required to produce the broad distributions implied by the magnitude of the experimentally–observed effects.²⁸ The broad non–thermal populations photoexcited here create a fs charge imbalance that, for $T_1 \leq 100\text{fs}$, follows the laser pulse and also contributes to demagnetization. Both “longitudinal” (demagnetization) and “transverse” (re–orientation) fs spin dynamics arise from the competition of spin–orbit and magnetic–exchange interactions described here. However, they manifest themselves differently for different photoexcitation conditions and external magnetic fields. For example, fs demagnetization (decrease in Mn spin amplitude) through dynamical polarization of longitudinal hole spins dominates for high fluences of 100s of $\mu\text{J}/\text{cm}^2$.²¹ By using pulse–trains, we may achieve spin rotational switching with lower pump intensities, which reduces the fs demagnetization.

As already shown in Fig. 5, by coherently controlling the non–thermal population imbalance between the four exchange–split HH and LH bands, we can control the direction of out–of–plane $\Delta S_z/S$. This is seen more clearly in Figs. 6(b) and (c), which show the frequency–dependence of $\Delta S_z/S$ and compare its individual contributions obtained by retaining one valence band at a time. The non–equilibrium population of band states with different spin admixtures leads to different directions of laser–induced spin–canting $\Delta S_z(t)$, which allows for magnetization control via pump frequency tuning. For example, photoholes excited in the two exchange–split (HH or LH) valence bands may induce opposite out–of–plane tilts. The finite pulse–duration and non–parabolic band dispersion (Appendix B and Fig. 1(a)) lead to different populations of more than one bands and BZ directions at all frequencies. As already discussed, such populations and spin–orbit interactions differ between $\hbar\omega_p \sim 1.5\text{eV}$ and $\hbar\omega_p \sim 3\text{eV}$ due to the difference in bandstructure. As seen by comparing Figs. 6(b) and (c), the bandstructure close to the Fermi level, where all $\{100\}$, $\{110\}$, and $\{111\}$ symmetry directions are populated, leads to order of magnitude smaller $\Delta S_z/S$ as compared to the high– \mathbf{k} bands along $\{111\}$ excited for $\hbar\omega_p \sim 3\text{eV}$. This theoretical result is consistent with the difference in order of magnitude of photoexcited spin and populations observed experimentally between the two above frequencies.^{36,37} We conclude that optical control of the photoexcited carrier populations can be used to switch the directions of photoexcited fs spin–orbit torques and, in this way, control the direction of fs magnetization canting at different laser frequencies.

The precise magnitude of the proposed effects depends on the relaxation timescales. The non–thermal populations are created during the 100fs laser pulse via $e-h$ optical polarization. Following dephasing after T_2 , these photocarriers relax on a timescale T_1 . The above characteristic relaxation times are expected to be in the 10–200fs range in (Ga,Mn)As.^{21,51} For pump fluences of

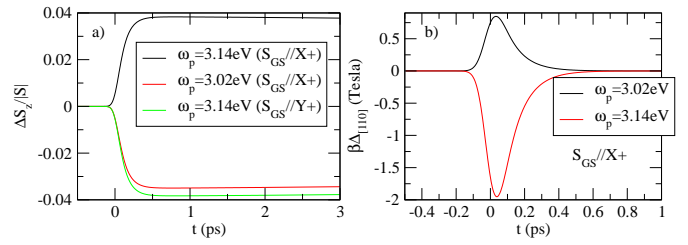


FIG. 7: (Color online) Calculated fs spin dynamics similar to Fig. 5 but with order of magnitude higher pump fluence $\sim 100\mu\text{J}/\text{cm}^2$. (a) Comparison of out–of–plane magnetization components for two different initial magnetic states and ω_p . (b) Photohole fs anisotropy fields along $[110]$ for the two ω_p .

$\sim 10\mu\text{J}/\text{cm}^2$, the experiment gives $\Delta S_z/S \sim 0.5\%$, reproduced by our theory for $T_1=100\text{fs}$ and $T_2=50\text{fs}$. This spin tilt decreases to $\Delta S_z/S \sim 0.01\%$ as T_2 decreases to 3fs with fixed $T_1=100\text{fs}$. For fixed short $T_2=10\text{fs}$, $\Delta S_z/S$ varies between 0.05–0.1% as T_1 varies between 30fs and 100fs. In all cases, we conclude that the fs spin–orbit torque contribution has the same order of magnitude as the experimental results unless T_1 and T_2 are few fs or less. From now on we fix $T_1=100\text{fs}$ and $T_2=50\text{fs}$.

The non–thermal fs spin–orbit torque contribution can be enhanced by increasing the laser intensity. Fig. 7(a) shows that, for easily attainable $\sim 100\mu\text{J}/\text{cm}^2$ low pump fluences,³⁷ the “sudden” magnetization tilt increases to $\Delta S_z/S \sim 4\%$ (for $E_0=7 \times 10^5\text{V}/\text{cm}$). Fig. 7(b) then shows that $\beta\Delta S_h(t)$ along $[110]$ grows into the Tesla range. The precise magnitude of this fs magnetization canting is sample–dependent and depends on relaxation. The different intensity–dependence and temporal profiles of the thermal and coherent/non–thermal carrier–spin components distinguishes these two contributions to the photoexcited spin. While the quasi–equilibrium contribution \mathbf{H}_{FS} is limited by the chemical potential, ΔS_h is controlled by the laser frequency. A distinct impulsive component of fast magnetic anisotropy was observed in the ps magnetization trajectory measured in Ref. [37] for pump fluences above $\sim 70\mu\text{J}/\text{cm}^2$ at $\hbar\omega_p \sim 1.5\text{eV}$. Fig. 7(a) also compares the spin canting dynamics for initial magnetization along the X_0^+ or Y_0^+ easy axis for $B=0$. Similar to the experiment of Fig. 4(d), it displays symmetric temporal profiles of $\Delta S_z(t)$, with opposite signs for the two perpendicular easy axes. In this way, we can distinguish the two magnetic states within 100fs. The equal magnitude of ΔS_z between the two perpendicular in–plane easy axes arises from the diagonal direction of ΔS_h for $\Delta_{pd}/\Delta_{so} \sim 1/3$ as in (Ga,Mn)As (Fig. 2). The overall agreement between theory and experiment suggest that a magnetic state can be read within 100fs, by monitoring the direction of out–of–plane laser–induced magnetization canting.

The above theory–experiment comparison of fs magnetism and the connection of Fig. 6(b) to other ps–resolved magneto–optical experiments³⁷ make a case

that optical control of a short-lived coherent population imbalance between exchange-split, spin-orbit-coupled anisotropic bands can generate fs spin-orbit torque with controllable direction, temporal profile, and magnitude. The latter initiates “sudden” magnetization dynamics. This result is not specific to the (Ga,Mn)As four-state magnetic memory but may also apply to other magnetic materials with strong spin-orbit coupling^{9,10} and uniaxial magnetic anisotropy. In (III,Mn)V ferromagnets, we are not aware of any experiment so far showing non-thermal laser-induced 360° switchings between multiple magnetic states. This may be due to the fact that a 100fs laser pulse not only excites magnon oscillations around the equilibrium easy axis but, even for low $\sim 10\mu\text{J}/\text{cm}^2$ fluences, also induces undesired fs electronic heating of spins.^{28,29} A complete quenching of ferromagnetism in (III,Mn)V has been reported for pump fluences on the mJ/cm^2 range.^{8,29} Our calculations show that, with a single 100fs pulse, similarly high fluences are required to induce a sufficiently strong “initial condition” $\Delta\mathbf{S}(t)$ that achieves switching to a different magnetic state. Below we show that, alternatively, pulse-shaping²³ can be used to initiate switching in a more controlled way, while keeping the *peak* laser fluence per pulse as low as possible to reduce fs electronic heating. In this way we may maximize the “transverse” hole spin excitations while reducing the “longitudinal” demagnetization by keeping the pump fluence per pulse in the 10–100 $\mu\text{J}/\text{cm}^2$ range.

A more general message conveyed by our theory-experiment results is that laser-driven dipolar coupling mediated by spin-orbit fluctuations in *pd*-coupled ferromagnetic ground states favors local spin canting during fs optical excitation. Interestingly, in strongly correlated electron materials such as colossal magneto-resistive manganites, laser-driven dipolar bonding mediated by quantum spin-flip fluctuations was shown to induce local spin canting in an antiferromagnetic ground state.^{1,4} This quantum spin canting was shown to drive a magnetic phase transition during $<100\text{fs}$ laser pulses.¹ Such *quantum femtosecond magnetism* originates from transient modification of the inter-atomic hopping of valence electrons by the laser E-field, which non-adiabatically generates spin-exchange coupling and ferromagnetic correlation as photoelectrons hop while simultaneously flipping local spins. Such results point to a more universal behavior: laser-induced dipolar coupling mediated by spin-dependent valence fluctuations favors spin-symmetry-breaking even during the highly non-equilibrium and non-thermal femtosecond timescales.

IV. INITIATING DETERMINISTIC SWITCHINGS WITH A LASER-PULSE-TRAIN

Results so far imply that a single 100fs laser pulse with $\sim 10\text{--}100\mu\text{J}/\text{cm}^2$ fluence excites magnon oscillations around the equilibrium easy axis. Switching of the magnetization to a different magnetic state requires photoex-

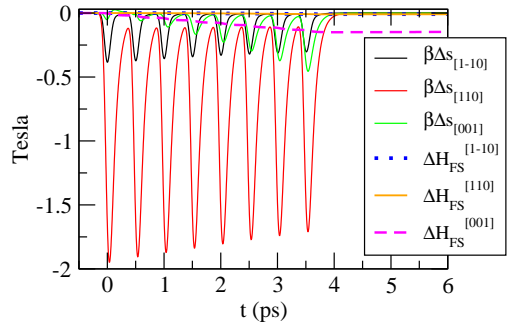


FIG. 8: (Color online) Comparison of non-thermal and quasi-thermal components of laser-induced magnetic anisotropy fields $\beta\Delta\mathbf{s}_h(t)$ and $\Delta\mathbf{H}_{FS}(t)$ during coherent nonlinear photoexcitation with a train of $N=8$ 100fs laser pulses separated by 500fs, with $E_0=7\times 10^5\text{V}/\text{cm}$ and $\hbar\omega_p=3.14\text{eV}$.

citation of a stronger “initial condition” $\Delta\mathbf{S}(t)$. While switching via thermally assisted processes may be possible by increasing the fluence to the mJ/cm^2 range,³⁸ pulse-shaping²³ can initiate switching in a more controlled way while keeping the laser fluence per pulse in the $\mu\text{J}/\text{cm}^2$ range to reduce fs electronic heating of spins. Here we coherently control $\Delta\mathbf{s}_h(t)$ by using M time-delayed laser pulse-trains, each consisting of N Gaussian pulses with duration $\tau_p=100\text{fs}$. The optical field is

$$\mathbf{E}(t) = \sum_{j=1}^M \mathbf{E}_0 \sum_{i=1}^N \exp[-(t - \tau_j - \Delta\tau_{ij})^2 / \tau_p^2] \times \exp[-i\omega_p^{(j)}(t - \tau_j - \Delta\tau_{ij})]. \quad (14)$$

Here we tune τ_j , the time delay of the j -th laser-pulse-train, and $\omega_p^{(j)}$, the pulse-train central frequency, but fix $\Delta\tau_{ij}=500\text{fs}$ for simplicity. In this section we consider $M=1$ and control the net duration of the spin-orbit torque with a single train of N laser pulses. In Fig. 8 we compare the components of $\beta\Delta\mathbf{s}_h(t)$ and $\gamma\Delta\mathbf{H}_{FS}$ obtained for $N=8$ in the coordinate system defined by the [110], [1-10], and [001] directions. We use the same $\sim 100\mu\text{J}/\text{cm}^2$ fluence as in Fig. 7. The non-thermal contribution $\beta\Delta\mathbf{s}_h(t)$ prevails over the thermal contribution $\Delta\mathbf{H}_{FS}(t)$, which builds-up as $\Delta\mathbf{s}_h$ drives $\Delta\mathbf{S}(t)$ and forces the spin of the Fermi sea bath to adjust to the new direction of $\mathbf{S}(t)$.¹⁷ This $\Delta\mathbf{S}(t)$ builds-up in a step-by-step fashion well before relaxation, driven by a sequence of successive photoexcited fs spin-orbit torques.

$\Delta\mathbf{H}_{FS}(t)$ originates from the spin of the thermal hole Fermi sea and is therefore restricted by the Fermi-Dirac distribution. The latter thermal populations give anisotropy fields of the order of few 10’s of mT in (Ga,Mn)As,^{6,37} as they are restricted by the equilibrium anisotropy parameters and $\sim\mu\text{eV}$ free energy differences with \mathbf{S} . On the other hand, the experiments observe anisotropy fields that are at least one order of magnitude larger.^{36,37} Fig. 8 compares the thermal

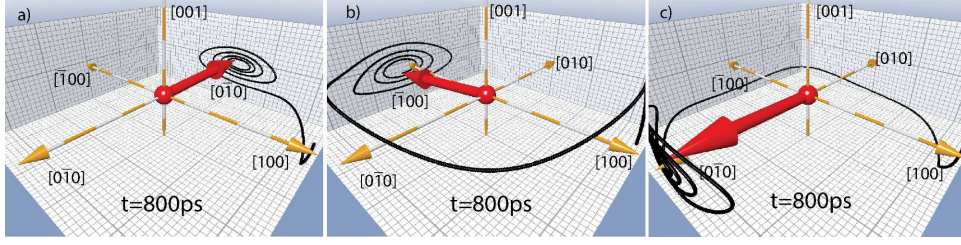


FIG. 9: (Color online) Magnetization switching trajectories from X^+ to the other three magnetic states, controlled by tuning the frequency ω_p and triggered by a single laser-pulse train with increasing number of pulses N and $E_0=7\times 10^5$ V/cm. All switchings are followed by pronounced magnetic ringing. (a): Counter-clockwise switching $X^+ \rightarrow Y^+$, initiated by HH photoexcitation with $N=7$ pulses. (b): 180° magnetization reversal via clockwise pathway $X^+ \rightarrow Y^- \rightarrow X^-$, initiated by LH photoexcitation with $N=9$ pulses. (c): Photoexcitation as in (a), but with $N=12$ pulses. By increasing N , the magnetization moves past the Y^+ and X^- intermediate states and accesses the Y^- state via the 270° counter-clockwise pathway $X^+ \rightarrow Y^+ \rightarrow X^- \rightarrow Y^-$.

anisotropy field $\Delta \mathbf{H}_{FS}(t)$ to the non-thermal photohole contribution $\beta \Delta \mathbf{s}_h(t)$ obtained at $\hbar\omega_p \sim 3.1$ eV for the $\sim 100 \mu\text{J}/\text{cm}^2$ pump fluence used in Ref. [37]. This non-thermal photohole spin was calculated in the time-domain by solving density matrix equations of motion after taking into account the (Ga,Mn)As bandstructure at 3.1 eV. For $\hbar\omega_p \sim 1.5$ eV, a similar calculation shown in Fig. 6(b) gives smaller photoexcited spin due to the different bandstructure and populated BZ directions close to the Fermi level. In our calculations, the photoexcited populations are not restricted by the Fermi-Dirac distribution. By tuning the laser frequency, the photocarriers can populate non-parabolic anisotropic parts of the BZ that cannot be accessed close to quasi-equilibrium. Our quantum kinetic calculation far from equilibrium gives more flexibility as compared to assuming quasi-equilibrium changes in the temperature and chemical potential, which are only established after a short but finite time T_1 . As seen in Fig. 8, $\beta \Delta \mathbf{s}_h(t)$ can grow to ~ 2 T along [110] for experimentally-relevant pump fluences and $T_1 \sim 100$ fs. For such fast photocarrier relaxation, $\Delta \mathbf{s}_h(t)$ follows the laser-pulse-train temporal profile and the relative phase of consecutive pulses does not play a role. However, $\Delta \mathbf{s}_h(t)$ is not the same for different pulses, as the non-equilibrium electronic states change non-adiabatically with $\Delta \mathbf{S}(t)$ (Appendix A).

We now show that, by increasing N , we can initiate switching rotation to any one of the available magnetic states. Fig. 9 shows three such magnetization switching trajectories up to long times $t=800$ ps. These ps trajectories are initiated at $t=0$ by $N=7$ (Fig. 9(a)), $N=9$ (Fig. 9(b)), or $N=12$ (Fig. 9(c)) pulses with $\sim 100 \mu\text{J}/\text{cm}^2$ fluence. By increasing N , we can switch from X^+ to all three other magnetic states Y^+ , X^- , and Y^- . In Fig. 9(a), $N=7$ pulses with $\hbar\omega_p=3.02$ eV (HH photoexcitation) initiate a counter-clockwise 90° switching rotation that stops after reaching the next magnetic state, Y^+ , within ~ 80 ps. The magnetization oscillates around the final state with a significant amplitude that cannot be controlled with a single pulse-train (magnetic ringing).⁴⁷ This ringing results from the weak (nanosecond) Gilbert damping of the local-spin precession observed in an-

nealed (Ga,Mn)As.^{33,37} While magnetic ringing can make multiple 90° switchings unstable, below we show that we can suppress it by exerting opposing fs spin-orbit torques. By increasing the number of pulses to $N=9$, the magnetization continues past Y^+ to the next available state, X^- . Fig. 9(b) then shows magnetization reversal via clockwise instead of counter-clockwise rotation, since $\hbar\omega_p=3.14$ eV excites e -LH instead of e -HH optical transitions. This $X^+ \rightarrow Y^- \rightarrow X^-$ pathway completes within ~ 150 ps and is again followed by magnetic ringing. By increasing the number of pulses to $N=12$, the fs spin-orbit torque is sufficient to move the magnetization even beyond X^- . Fig. 9(c) shows 270° switching to the Y^- state within ~ 200 ps, following a $X^+ \rightarrow Y^+ \rightarrow X^- \rightarrow Y^-$ pathway initiated by e -HH photoexcitation.

V. OPTICAL CONTROL OF SEQUENTIAL 90° SWITCHINGS BETWEEN FOUR STATES

In this section we provide an example of how our proposed optical manipulation of fs spin-orbit torques could be used to gain full access of a four-state magnetic memory. Fig. 10 shows two switching protocols that achieve 360° control of the magnetic states of Fig. 1(b). The upper panel shows the sequences of laser-pulse-trains used to control the four sequential 90° switchings. Two different laser frequencies excite e -HH or e -LH optical transitions, which allow us to stop and restart the magnetization motion at each of the four magnetic states as desired. By tuning the laser frequency we choose the direction of fs spin-orbit torques and multi-step switching process, which takes place via counter-clockwise (Fig. 10(a)) or clockwise (Fig. 10(b)) magnetization rotations forced to stop at all intermediate states at will. To control the photoexcited $\Delta \mathbf{s}_h(t)$ and fs spin-orbit torques, we turn three experimentally accessible “knobs”: (i) *Pulse-shaping*²³ by changing N , which controls the net duration and temporal profile of the spin-orbit torques. In this way, we tailor $\Delta \mathbf{S}(t)$ that initiates or modifies the switching rotations with low intensity per laser pulse. (ii) *Frequency-tuning* enables selective photoexcitation of

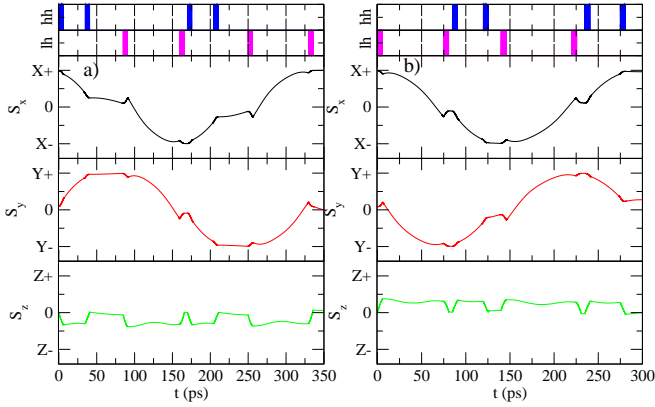


FIG. 10: (Color online) Two protocols for 360° control of the full four-state magnetic memory via four sequential 90° switchings that stop and restart at each intermediate magnetic state. (a) Counter-clockwise sequence $X^+ \rightarrow Y^+ \rightarrow X^- \rightarrow Y^- \rightarrow X^+$, (b) Clockwise sequence $X^+ \rightarrow Y^- \rightarrow X^- \rightarrow Y^+ \rightarrow X^+$. Upper panel: Timing sequences and colors of the laser-pulse-trains ($N=12$) that create the needed fs spin-orbit torque sequences. Blue pulses excite HH optical transitions, magenta pulses excite LH transitions. $E_0=7 \times 10^5 \text{ V/cm}$ (pump fluence of $\approx 100 \mu\text{J/cm}^2$).

exchange-split LH or HH non-equilibrium populations with different superpositions of spin- \uparrow and spin- \downarrow states. In this way we control the population imbalance that decides the directions of $\Delta\mathbf{s}_h$, fs spin-orbit torque, and $\Delta\mathbf{S}(t)$. (iii) By controlling the *time-delays* τ_j , we exert fs spin-orbit torques at desirable times in order to stop and restart the switching rotation at all intermediate states and suppress magnetic ringing. This is discussed further in the next section. To understand the role of the twelve laser-pulse-trains chosen in Fig. 10, we note the following points: (i) a laser-pulse-train initiates switchings or magnon oscillations via fs spin-orbit torque with direction that depends on *both* laser frequency and magnetic state, (ii) when the magnetization reaches a new magnetic state, we use a laser-pulse-train to exert opposing fs spin-orbit-torques, in a direction that stops the switching rotation and suppresses the magnetic ringing so that we can access the state, and (iii) when we are ready to move on, a laser-pulse-train with the appropriate color restarts the 360° switching process by exerting fs spin-orbit torques in the desirable direction.

Fig. 10 shows four sequential 90° switchings controlled by $\Delta\mathbf{s}_h(t)$. In Fig. 10(a), a counter-clockwise $X^+ \rightarrow Y^-$ switching is initiated by e -HH photoexcitations with $N=12$ pulses. After $\tau=35\text{ps}$, the magnetization reaches the vicinity of the intermediate Y^+ state. We then stop the switching process by exciting e -HH optical transitions. We restart the motion at $\tau=85\text{ps}$, after waiting for about 50ps , by using e -LH photoexcitations to switch the magnetization to the X^- state. There we again stop the process at $\tau=160\text{ps}$, by exciting e -LH optical transitions. We restart at $\tau=170\text{ps}$ with

e -HH photoexcitations, which trigger switching to Y^- . This switching completes within $\sim 35\text{ps}$, after we stop the motion with e -HH photoexcitations at $\tau=205\text{ps}$. We finish the 360° switching loop by using e -LH photoexcitations to restart the counter-clockwise motion back to X^+ , at $\tau=250\text{ps}$, and later to terminate the process at $\tau=330\text{ps}$. Fig.10(b) shows an opposite clockwise switching sequence $X^+ \rightarrow Y^- \rightarrow X^- \rightarrow Y^+ \rightarrow X^+$, obtained by changing the laser-pulse frequencies from e -HH to e -LH excitations and vice-versa. In this case, e -LH optical transitions with $N=12$ pulses trigger clockwise magnetization rotation, which we suppress at Y^- with LH excitations at $\tau=75\text{ps}$. We restart the process with e -HH photoexcitation at $\tau=85\text{ps}$ and suppress it again at X^- with e -HH optical transitions at $\tau=120\text{ps}$. We restart with e -LH excitation at $\tau=140\text{ps}$ and switch to Y^+ , where we suppress the motion at $\tau=225\text{ps}$ with e -LH optical transitions. We complete a closed switching loop to the initial X^+ state with e -HH photoexcitation at $\tau=235\text{ps}$ and suppress the rotation with e -HH optical transitions at $\tau=275\text{ps}$. In the next section we analyze how tunable fs spin-orbit torque direction offers more flexibility for controlling switching rotations and magnetic ringing.

VI. CONTROLLING MAGNETIC SWITCHING AND RINGING WITH A LASER-PULSE-TRAIN

While the optical control scheme via fs spin-orbit torque discussed in the previous section allows for elaborate switching of a multi-state magnetic memory, it may also apply to conventional memories exhibiting uniaxial magnetic anisotropy. Its main advantage, in addition to initiating selective switchings and flipping the spin between two states, is that it can suppress the magnetization motion and magnetic ringing at any time, at any intermediate magnetic state. Magnetic ringing arises from the weak damping of the magnetization precession around an easy axis following excitation with either optical or magnetic field pulses and limits the read/write times in many magnetic materials.⁴⁷ One known way to reduce it is to take advantage of the phase $\Omega\tau$ of magnetization precession with frequency Ω .^{34,47} With magnetic field pulses, this can be done by adjusting the duration of a long pulse to the precession period.⁴⁷ With ultrashort laser pulses, one can suppress (enhance) the precession by exciting when $\Omega\tau=\pi$ ($\Omega\tau=2\pi$) in the same way as at $\tau=0$.³⁴ Such coherent control of spin precession is possible for harmonic oscillations. Below we show that we can optically control both magnon oscillations and nonlinear switching rotations by applying clockwise or counter-clockwise fs spin-orbit torque pulse sequences when needed.

We start with the harmonic limit and demonstrate magnon control via fs spin-orbit torque with tunable direction. First we excite at $\tau=0$ magnon oscillations with frequency Ω (thick solid line in Fig. 11). We thus initiate magnetization precession around the X^+ (Fig. 11(a))

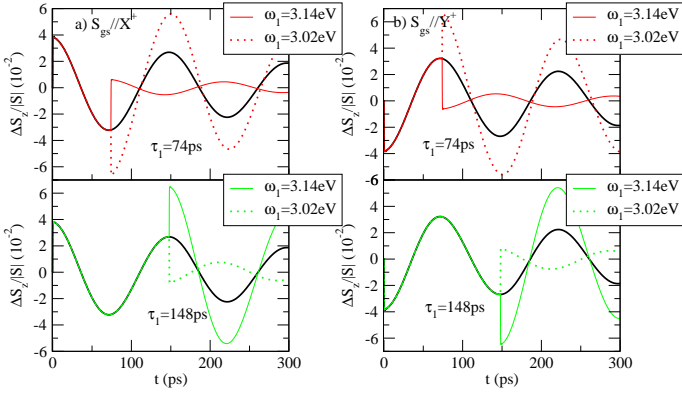


FIG. 11: (Color Online) Two 100fs laser pulses, delayed by τ , enhance or suppress magnon oscillations via fs spin-orbit torque. The first pulse, $\hbar\omega_p=3.14\text{eV}$, starts the precession (frequency Ω) at $\tau=0$. The second pulse, $\hbar\omega_p = 3.02\text{eV}$ or $\hbar\omega_p = 3.14\text{eV}$, arrives at $\tau=74\text{ps}$ ($\Omega\tau=\pi$) or $\tau=148\text{ps}$ ($\Omega\tau=2\pi$). Equilibrium magnetic state: (a): X^+ and (b): Y^+ .

or the Y^+ (Fig. 11(b)) easy axis with e -LH excitation ($\hbar\omega_p=3.14\text{eV}$). An impulsive magnetization at $\tau=0$ is observed in the ps trajectory of Fig. 11. The initial phase of these magnon oscillations is opposite between the X_0^+ and Y_0^+ states, due to the opposite directions of the fs spin-orbit torques (Fig. 7(a)). We then send a control laser pulse at $\tau=74\text{ps}$ ($\Omega\tau=\pi$) or at $\tau=148\text{ps}$ ($\Omega\tau=2\pi$), but use either $\hbar\omega_p=3.14\text{eV}$ (e -LH optical transitions) or $\hbar\omega_p=3.02\text{eV}$ (e -HH optical transitions). By controlling the direction of fs spin-orbit torque with such frequency tuning, we show that we can both enhance and suppress the amplitude of the magnetization precession at *both* $\Omega\tau=\pi$ and $\Omega\tau=2\pi$. While for $\Omega\tau=\pi$ we suppress the magnetic ringing when applying the same fs spin-orbit torque as for $\tau=0$ ($\hbar\omega_p=3.14\text{eV}$), we can also enhance it by applying an opposite fs spin-orbit torque ($\hbar\omega_p=3.02\text{eV}$). Similarly, at time $\Omega\tau=2\pi$, we enhance the ringing when applying fs spin-orbit torque in the same direction as for $\tau=0$ and suppress it by reversing the direction. We thus gain flexibility in both starting and stopping magnon oscillations.

Unlike for harmonic precession, switching also involves nonlinearities and anharmonic effects. In Fig. 12(a), a $X^+ \rightarrow Y^+ \rightarrow X^- \rightarrow Y^-$ switching pathway (dashed line) is initiated at $\tau=0$ as in Fig. 9(c). After about 200ps, the magnetization switches to Y^- , after overcoming the intermediate states Y^+ and X^- . The X-component of the magnetization then oscillates with significant amplitude (magnetic ringing, see dashed curve in Fig. 12(a)). Fig. 12(a) (solid curve) demonstrates suppression of this ringing by a control laser-pulse-train that can arrive at any time after the switching is completed. To accomplish this, we tune the direction, duration, and strength of the exerted fs spin-orbit torques. Figs. 12(b) and (c) show that the control pulse-train can also stop the $X^+ \rightarrow Y^+ \rightarrow X^- \rightarrow Y^-$ switching at one of the intermediate magnetic states before reaching Y^- . However, we

must use different ω_p at Y^+ and X^- in order to get an opposing fs spin-orbit torque, as the direction of the latter depends on the magnetic state. In Fig. 12(b) we stop the switching at the X^- magnetic state, after passing through Y^+ , by exciting with $\hbar\omega_p=3.14\text{eV}$ at $\tau\sim 100\text{ps}$ (e -LH photoexcitation). Fig. 12(c) shows that we can stop at Y^+ after $\sim 35\text{ps}$, by exerting a clockwise spin-orbit torque using $\hbar\omega_p=3.02\text{eV}$ (HH photoholes). A more dramatic demonstration of the flexibility offered by fs spin-orbit torque is given in Fig. 12(d). Here we initiate the $X^+ \rightarrow Y^-$ switching as above and then stop it immediately, by applying a control laser-pulse-train at $\tau=2\text{ps}$, i.e. long before any oscillations can develop. Instead of relying on the precession phase as in Fig. 11, we apply a sufficiently strong clockwise fs spin-orbit torque that opposes the magnetization motion. In this way, we stop the magnetization at its tracks, after a minimal motion without oscillations. We conclude that coherent optical control of the mobile spin excited during fs laser pulses allows us to suppress both magnetic ringing and non-linear switching rotations, by controlling the direction, duration, and magnitude of fs spin-orbit torques.

VII. CONCLUSIONS AND OUTLOOK

In this paper we used density-matrix equations of motion with bandstructure to describe photoexcitation and frequency-dependent control of fs spin-orbit torques analogous to the static current-induced ones in spintronics. In this all-optical way, we initiate, stop, and control multiple magnetic switchings and magnetic ringing. The proposed non-adiabatic mechanism involves optical control of direction, magnitude, and temporal profile of fs spin-orbit torque sequences. This is achieved by tuning, via the optical field, a short-lived carrier population and spin imbalance between exchange-split bands with different spin-orbit interactions. The photoexcited spin magnitude and direction depend on symmetry-breaking arising from the non-perturbative competition of spin-orbit and spin-exchange couplings of coherent photoholes. We validated our initial prediction of fs spin-orbit torque³ by comparing our calculations to existing magneto-optical pump-probe measurements monitoring the very early $\sim 100\text{fs}$ temporal regime following excitation with a single linearly-polarized laser pulse. The most clear experimental signature is the observation of laser-induced fs magnetic hysteresis and switching of the direction of out-of-plane femtosecond magnetization component with magnetic state. Such magnetic hysteresis is absent without pump, while static planar Hall effect measurements observe similar in-plane switchings in the transverse component of the Hall magnetoresistivity. The observation of switching of laser-induced fs transverse magnetization with magnetic state cannot arise from longitudinal nonlinear optical effects and demagnetization/amplitude changes. The dependence on magnetic state indeed disappears with increasing perpendic-

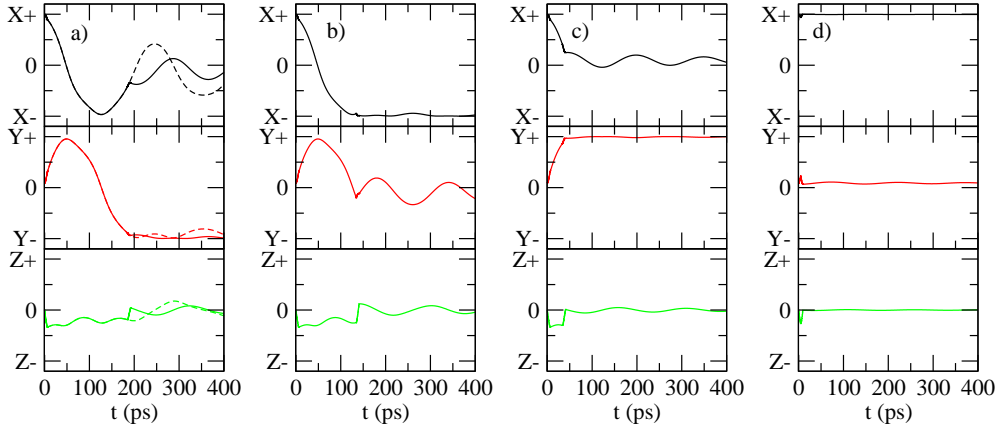


FIG. 12: (Color online) Time-dependence of magnetization components controlled by a time-delayed fs spin-orbit torque pulse train. (a): $X^+ \rightarrow Y^+ \rightarrow X^- \rightarrow Y^-$ switching pathway is initiated at $\tau=0$ with HH photoexcitation (dashed line). After switching completes, the unavoidable magnetic ringing is reduced by a control laser-pulse-train that can exert opposing fs spin-orbit torques at any time (solid line). (b): The $X^+ \rightarrow Y^-$ switching of (a) is terminated by opposing fs spin-orbit torques after magnetization reversal to X^- . (c): The $X^+ \rightarrow Y^-$ switching is terminated by a control laser-pulse-train after 90° rotation to Y^+ . (d): The $X^+ \rightarrow Y^-$ switching is stopped immediately after it is initiated, by opposing fs spin-orbit torque at $\tau=2$ ps.

ular magnetic field, which suppresses the magnetization re-orientation. In this way we can separate experimentally longitudinal and transverse femtosecond magnetization changes. We discussed two theoretical results that may be useful for coherent control of magnetic memory states and magnetic ringing via fs spin-orbit torque: (i) We showed that femtosecond optical excitation can start, stop, and restart switching pathways between the adiabatic free energy magnetic states in any direction. Based on this, we gave an example of sequences of laser-pulse trains that can provide controlled access to four different magnetic states via consecutive 90° switchings, clockwise or counter-clockwise. (ii) We demonstrated optical control of magnon oscillations and switching rotations and suppression of magnetic ringing at any time, long or short. For this we enhance spin-orbit torque via pulse-shaping and control its direction via laser frequency.

The full non-thermal control of a magnetic memory demonstrated here requires the following: (i) The competition between spin-orbit and magnetic exchange couplings breaks the symmetry while the laser electric field couples to the material. As a result, $e-h$ pair excitations are photoexcited with finite spin. There is no need to transfer angular-momentum from the photons (no circular polarization) since spin-orbit coupling does not conserve spin. (ii) The direction, magnitude, and duration of the non-thermal carrier spin-pulse is coherently controlled by the optical field. In particular, the direction of photoexcited spin is controlled by the laser frequency, the magnetic state, and the symmetry-breaking. Importantly, its magnitude increases with laser intensity and \mathbf{E}^2 , while its temporal profile follows that of the laser pulse if relaxation is sufficiently fast. Such characteristics of fs spin-orbit torque can distinguish it from adiabatic free energy effects. (iii) The photoexcited spin-pulses exert fs spin-orbit-torques on the collective local spin and

move it “suddenly”, in a controllable direction that depends on the magnetic state and the laser frequency. By coherently controlling the non-thermal population imbalance of exchange-split carrier bands with different spin-orbit interactions, we can move the local spin via non-adiabatic interaction with mobile spins. (iv) Laser-pulse-shaping²³ and increased pump-fluence allow us to access optically the magnetic nonlinearities of the carrier free energy. In this way, we may initiate or modify, during fs timescales, deterministic switchings to any available magnetic state. (v) By using control pulse-trains with appropriate frequencies, we suppress and restart switching rotations at intermediate magnetic states and suppress magnetic ringing after switchings complete. While coherent suppression of magnon oscillations is possible by taking advantage of the precession phase, here we mainly rely on controlling the direction of fs spin-orbit torque with respect to the direction of magnetization rotation. In this way we suppressed and enhanced both switching rotations and ringing at long and short times.

To control the entire four-state memory as in Fig. 10, we had to use time-delayed laser-pulse-trains with different frequencies at different magnetic states. The first excitation suppresses the switching rotation/ringing in order to access the state, while the second excitation restarts the process and moves the magnetization to the next magnetic state in the desired direction. While such control of the magnetization trajectory occurs on the 100fs timescale of coherent photoexcitation, the initiated deterministic switchings complete on ~ 100 ps timescales, as determined by the free energy and micromagnetic parameters. In a massively-parallel memory, we can control n different bits simultaneously on the 100fs timescale without waiting for each switching to complete. For large n , this would ideally result in memory reading and writing at ~ 10 THz speeds.

Our proposed fs spin-orbit torque mechanism may be relevant to different unexplored spin-orbit coupled materials with coexisting mobile and local carriers,¹¹ for example topological insulators doped with magnetic impurities.^{9,10} Important for practical implementations and experimental proof of fs spin-orbit torque is to identify materials where the quasi-thermal/adiabatic and non-thermal/non-adiabatic contributions to the magnetic anisotropy can be distinguished experimentally. It is possible to separate these two based on their temporal profiles and their dependence on photoexcitation intensity, laser frequency, and external magnetic field. In (Ga,Mn)As, Fig. 4 shows photogeneration of a “sudden” magnetization re-orientation and fs magnetic hysteresis for magnetic field perpendicular to the sample plane. Such magnetic field cants the ground state magnetization out of the plane, from $S_z=0$ ($B=0$) to $S_z \approx \pm S$ (large B). When $S_z \approx 0$ in equilibrium, $\Delta S_z(t)$ measures transverse magnetization re-orientation and magnetic hysteresis correlated with in-plane switching, while when $S_z \approx S$ longitudinal changes dominate $\Delta S_z(t)$ and there is no hysteresis. In this way, a perpendicular magnetic field can be used to elucidate the physical origin of the fs magneto-optical pump-probe signal dynamics. Distinct thermal and non-thermal contributions to the ps magnetization trajectory were also observed experimentally at $\hbar\omega_p \sim 1.5\text{eV}$.³⁷ They were separated based mainly on pump fluence dependence and by controlling the material’s micromagnetic parameters. Qualitative differences in the magnetization trajectory were observed above $\sim 70 \mu\text{J}/\text{cm}^2$ pump fluence. Below this, the easy axis rotates smoothly inside the plane, due to laser-induced temperature increase during $\sim 10\text{ps}$ timescales.^{33,37} Above $\sim 70 \mu\text{J}/\text{cm}^2$, a sub-picosecond “sudden” magnetization component is clearly observed.^{33,37} Importantly, while the precession frequency γH_{FS} increases linearly with equilibrium temperature, it saturates with pump fluence above $\sim 70 \mu\text{J}/\text{cm}^2$, even though the impulsive out-of-plane magnetization tilt continues to increase.³⁷ In contrast, the pump-induced reflectivity increases linearly with pump intensity up to much higher fluences $\sim 150\text{--}200 \mu\text{J}/\text{cm}^2$,³⁷ which indicates non-thermal photocarriers. Here we suggest that the numerical results of Fig. 6(b), which show frequency-dependent fs spin photoexcitation for $\hbar\omega_p \sim 1.5\text{eV}$, may explain the “sudden” out-of-plane magnetization canting observed in Ref. [37]. This requires $\sim 100 \mu\text{J}/\text{cm}^2$ pump fluences consistent with our theory. Our results describe the initial condition that triggers relaxation not treated here.

In closing, we note that the discussed concepts are of more general applicability to condensed matter systems. The main idea is the possibility to tailor order parameter dynamics via optical coherent control of non-thermal carrier populations, as well as via charge fluctuations and interactions driven while the optical field couples to the material. The initial coherent excitation temporal regime may warrant more attention in various condensed matter systems.^{1,4} An analogy can be drawn

to the well-known coherent control of femtosecond chemistry and photosynthetic dynamics, where the photoproducts of chemical and biochemical reactions can be influenced by creating coherent superpositions of molecular states.⁶⁹ Similarly, in condensed matter systems, laser-driven e - h pairs (optical polarization) can tailor non-adiabatic “initial conditions” that drive subsequent phase dynamics governed by the adiabatic free energy. An analogy can also be drawn to parameter quenches studied in cold atomic gases. There, quasi-instantaneous quenches drive dynamics that, in some cases such as BCS superconductors, can be mapped to classical spin dynamics. Coherent dynamics of superconducting order parameters are now beginning to be also studied in condensed matter systems,^{70,71} and an analogy to the magnetic order parameter studied here is clear. Other examples include quantum femtosecond magnetism in strongly-correlated manganites,^{1,4} photon-dressed Floquet states in topological insulators,⁷² and the existence of non-equilibrium phases in charge-density-wave correlated systems.⁴⁸ Femtosecond nonlinear optical and THz spectroscopy⁷³ offers the time resolution needed to disentangle different order parameters that are strongly coupled in the ground state, based on their different dynamics after “sudden” departure from equilibrium.^{48,49} Multi-pulse switching protocols based on non-adiabatic quantum excitations can control non-equilibrium phase transitions, by initiating phase dynamics in a controllable way.^{1,4}

Note added to proof: After our paper was submitted, we became aware of a recent preprint on time-resolved magneto-optical measurements of the collective magnetization ultrafast dynamics in (Ga,Mn)As.⁷⁵ This experiment observed a strong pump-frequency-dependence of the magnetization precession above the semiconductor band-gap, which originates from the non-thermal holes photoexcited in the semiconductor band states similar to our theoretical predictions here. The experimental results reveal a systematic but complex sample-dependent frequency dependence, which differs between annealed and as-grown samples. The observed effect is consistent with our predictions in Fig. 6(b). For example, the quasi-thermal anisotropy effects predicted here (e.g. $\Delta \mathbf{H}_{FS}$ in Fig. 8) are mainly driven by the fs ΔS_z . The latter “sudden” magnetization mainly drives the laser-induced contribution to the quasi-thermal magnetic anisotropy field Eq. (A10) determining the precession frequency (especially for in-plane initial magnetization $S_z \approx 0$, as for small B -fields). While our present theory neglects any laser-induced changes in the magnetic anisotropy parameters that characterize the free energy $E_h(\mathbf{S})$, which add to our predicted effects, it suggests that the frequency-dependent initial femtosecond change ΔS_z may be important for explaining the frequency-dependence of the precession frequency determined by Eq. (A10). Note that the decay of $\Delta \mathbf{S}$, photoinduced during femtosecond time-scales due to magnetic exchange interaction with the non-thermal photo-

hole spin, decays slowly, as determined by the sample-dependent Gilbert damping that differs markedly between annealed and as-grown samples.³³

VIII. ACKNOWLEDGEMENTS

This work was supported by the EU Seventh Framework Programme (FP7-REGPOT-2012-2013-1) under grant agreement No. 316165, by the EU Social Fund and National resources through the THALES program NANOPHOS, by the Greek GSRT project ERC02-EXEL (Contract No. 6260), by the Greek Ministry of Education ARISTEIA-APPOLO, and by the National Science Foundation Contract No. DMR-1055352.

Appendix A: Fermi-Dirac/Adiabatic versus Non-thermal/Non-adiabatic Magnetic Anisotropy

In this appendix we discuss the two contributions to laser-induced anisotropy: non-thermal and quasi-thermal. The adiabatic/quasi-thermal contribution comes from relaxed Fermi-Dirac carriers. The non-adiabatic contribution comes from the coherent/non-thermal photoexcited carriers, whose populations increase with intensity during photoexcitation. In the initial stage, these non-thermal carriers come from the continuum of e - h excitations excited by the fs laser pulse, so they follow its temporal profile. At a second stage, they redistribute among the different \mathbf{k} and band states while also scattering with the Fermi sea carriers.

1. Non-thermal/non-adiabatic magnetic anisotropy

We use density matrix equations of motion and bandstructure to describe the femtosecond photoexcitation of short-lived photohole spin-pulses driven by four competing effects: (i) magnetic exchange interaction between local and mobile spins, (ii) spin-orbit coupling of the mobile carriers, (iii) coherent nonlinear optical processes, and (iv) fast carrier relaxation. The interplay of these contributions breaks the symmetry and excites a controllable fs magnetic anisotropy field due to non-thermal photocarriers. The photoexcited spin, Eq.(3), is expressed in terms of the electronic density matrix, which resolves the different band and \mathbf{k} -direction contributions. Density matrix equations of motion were derived for the time-dependent Hamiltonian $H(t)$, Eq. (8), with bandstructure treated within standard tight-binding and mean-field approximations. This Hamiltonian has fast and slow contributions. Its adiabatic part $H_b(\mathbf{S}_0)$, Eq. (4), depends on the slowly varying (ps) spin \mathbf{S}_0 . The eigenstates of $H_b(\mathbf{S}_0)$ describe electronic bands determined by periodic potential, spin-orbit, and adia-

batic magnetic exchange coupling. The latter interaction

$$H_{pd}(\mathbf{S}_0) = \beta c \mathbf{S}_0 \cdot \hat{\mathbf{s}}_h, \quad (\text{A1})$$

where $\hat{\mathbf{s}}_h$ is the hole spin operator, leads to exchange-splitting of the HH and LH semiconductor valence bands determined by the exchange energy $\Delta_{pd} = \beta c S$. It also modifies the direction of photoexcited spin, by competing with the spin-orbit coupling of the mobile carriers characterized by the energy splitting Δ_{so} of the spin-orbit-split valence band of the parent material (GaAs) at $\mathbf{k}=0$. By adding to the Hamiltonian carrier-carrier and carrier-phonon interactions, we can also treat relaxation, included here by introducing the non-thermal population relaxation time T_1 and the e - h dephasing time T_2 .

We describe the band eigenstates of the adiabatic electronic Hamiltonian $H_b(\mathbf{S}_0)$ by using the semi-empirical tight-binding model that reliably describes the GaAs bandstructure.⁵² Compared to the standard $\mathbf{k} \cdot \mathbf{p}$ effective mass approximation, this tight-binding approach allows us to also address states with large momenta \mathbf{k} . Such anisotropic and non-parabolic band states contribute for laser frequencies away from the band-edge. Following Ref. [52], we include the quasi-atomic spin-degenerate orbitals $3s$, $3p_x$, $3p_y$, $3p_z$, and $4s$ of the two atoms per GaAs unit cell and use the tight-binding parameter values of the Slater-Koster sp^3s^* model. As in Ref. [3], we add to this description of the parent material the mean-field coupling of the Mn spin, Eq.(A1), which modifies spin-mixing in a non-perturbative way. Similar to Ref. [52], we diagonalize the Hamiltonian $H_b = H_b^c + H_b^v$ to obtain the conduction (H_b^c) and valence (H_b^v) bands:

$$H_b(\mathbf{S}_0) = \sum_{\mathbf{k}n} \varepsilon_{\mathbf{k}n}^c \hat{e}_{\mathbf{k}n}^\dagger \hat{e}_{\mathbf{k}n} + \sum_{\mathbf{k}n} \varepsilon_{-\mathbf{k}n}^v \hat{h}_{-\mathbf{k}n}^\dagger \hat{h}_{-\mathbf{k}n}. \quad (\text{A2})$$

The eigenvalues $\varepsilon_{\mathbf{k}n}^c(\mathbf{S}_0)$ and $\varepsilon_{-\mathbf{k}n}^v(\mathbf{S}_0)$ describe the conduction and valence band energy dispersions.

While \mathbf{S}_0 varies on a ps timescale much slower than the laser-induced electronic fluctuations, the rapidly-varying (fs) part of the Hamiltonian $H(t)$, $\Delta H_{exch}(t) + H_L(t)$, drives “sudden” deviations from adiabaticity. $\Delta H_{exch}(t)$, Eq.(9), describes non-adiabatic interactions of photocarrier spins with the fs magnetization $\Delta \mathbf{S}(t)$ induced by fs spin-orbit torque. $H_L(t)$ describes the optical field dipole coupling within the rotating wave approximation:

$$H_L(t) = - \sum_{nm\mathbf{k}} d_{nm\mathbf{k}}(t) \hat{e}_{\mathbf{k}m}^\dagger \hat{h}_{-\mathbf{k}n}^\dagger + h.c., \quad (\text{A3})$$

where $d_{nm\mathbf{k}}(t) = \mu_{nm\mathbf{k}} \mathcal{E}(t)$ is the Rabi energy, $\mathcal{E}(t)$ is the pump electric field, and $\mu_{nm\mathbf{k}}$ is the dipole transition matrix element between the valence band n and the conduction band m at momentum \mathbf{k} . These dipole matrix elements also depend on \mathbf{S}_0 and are expressed in terms of the tight-binding parameters of $H_b(\mathbf{k})$ as in Ref. [74]:

$$\mu_{nm\mathbf{k}} = \frac{i}{\varepsilon_{m\mathbf{k}} - \varepsilon_{n\mathbf{k}}} \langle n\mathbf{k} | \nabla_{\mathbf{k}} H_b(\mathbf{k}) | m\mathbf{k} \rangle. \quad (\text{A4})$$

The density matrix $\langle \hat{\rho} \rangle$ obeys the equations of motion

$$i\hbar \frac{\partial \langle \hat{\rho} \rangle}{\partial t} = \langle [\hat{\rho}, H(t)] \rangle + i\hbar \frac{\partial \langle \hat{\rho} \rangle}{\partial t} \Big|_{relax}. \quad (\text{A5})$$

The hole populations and coherences between valence bands are given by the equation of motion

$$\begin{aligned} & i\hbar \partial_t \langle \hat{h}_{-\mathbf{k}n}^\dagger \hat{h}_{-\mathbf{k}n'} \rangle - (\varepsilon_{\mathbf{k}n'}^v - \varepsilon_{\mathbf{k}n}^v - i\Gamma_{nn'}^h) \langle \hat{h}_{-\mathbf{k}n}^\dagger \hat{h}_{-\mathbf{k}n'} \rangle \\ &= \sum_m d_{mn\mathbf{k}}^*(t) \langle \hat{h}_{-\mathbf{k}n'} \hat{e}_{\mathbf{k}m} \rangle - \sum_m d_{mn'\mathbf{k}}(t) \langle \hat{h}_{-\mathbf{k}n} \hat{e}_{\mathbf{k}m} \rangle^* \\ &+ \beta c \Delta \mathbf{S} \sum_l \left[\mathbf{s}_{\mathbf{k}n'l}^h \langle \hat{h}_{-\mathbf{k}n}^\dagger \hat{h}_{-\mathbf{k}l} \rangle - \mathbf{s}_{\mathbf{k}n'l}^{h*} \langle \hat{h}_{-\mathbf{k}l}^\dagger \hat{h}_{-\mathbf{k}n'} \rangle \right] \end{aligned} \quad (\text{A6})$$

where $n=n'$ describes the non-thermal populations and $n \neq n'$ the coherent superpositions of different valence band states. $\Gamma_{nn}^h = \hbar/T_1$ characterizes the non-thermal population relaxation. $\Gamma_{nn'}^h$ are the inter-valence-band dephasing rates, which are short and do not play an important role here. The first term on the rhs describes the photoexcitation of hole populations in band states (n, \mathbf{k}) that depend on \mathbf{S}_0 . The second term is beyond a simple rate equation approximation and describes the non-adiabatic changes in the hole states induced by their interaction with the rapidly varying (fs) photoinduced magnetization $\Delta \mathbf{S}(t)$, Eq.(9). Similarly,

$$\begin{aligned} & i\hbar \partial_t \langle \hat{e}_{\mathbf{k}n'}^\dagger \hat{e}_{\mathbf{k}n'} \rangle - (\varepsilon_{\mathbf{k}n'}^c - \varepsilon_{\mathbf{k}n}^c - i\Gamma_{nn'}^e) \langle \hat{e}_{\mathbf{k}n'}^\dagger \hat{e}_{\mathbf{k}n'} \rangle = \\ & \sum_{m'} d_{nm'm'\mathbf{k}}^* \langle \hat{h}_{-\mathbf{k}m'} \hat{e}_{\mathbf{k}n'} \rangle - \sum_{m'} d_{n'm'\mathbf{k}} \langle \hat{h}_{-\mathbf{k}m'} \hat{e}_{\mathbf{k}n} \rangle^* \end{aligned} \quad (\text{A7})$$

where the rates $\Gamma_{nn'}^e$ characterize the electron relaxation.

In the above equations of motion, the photoexcitation of the carrier populations and coherences is driven by the nonlinear e - h optical polarization $\langle \hat{h}_{-\mathbf{k}n} \hat{e}_{\mathbf{k}m} \rangle$ (off-diagonal density matrix element). This coherent amplitude characterizes the e - h excitations driven by the optical field, which here only exist during the laser pulse since their lifetime T_2 (dephasing time) is short:

$$\begin{aligned} & i\hbar \partial_t \langle \hat{h}_{-\mathbf{k}n} \hat{e}_{\mathbf{k}m} \rangle - (\varepsilon_{\mathbf{k}m}^c + \varepsilon_{\mathbf{k}n}^v - i\hbar/T_2) \langle \hat{h}_{-\mathbf{k}n} \hat{e}_{\mathbf{k}m} \rangle \\ &= -d_{mn\mathbf{k}}(t) \left[1 - \langle \hat{h}_{-\mathbf{k}n}^\dagger \hat{h}_{-\mathbf{k}n} \rangle - \langle \hat{e}_{\mathbf{k}m}^\dagger \hat{e}_{\mathbf{k}m} \rangle \right] \\ &+ \beta c \Delta \mathbf{S}(t) \cdot \sum_{n'} \mathbf{s}_{\mathbf{k}nn'}^h \langle \hat{h}_{-\mathbf{k}n'} \hat{e}_{\mathbf{k}m} \rangle \\ &+ \sum_{n' \neq n} d_{mn'n\mathbf{k}}(t) \langle \hat{h}_{-\mathbf{k}n'}^\dagger \hat{h}_{-\mathbf{k}n} \rangle \\ &+ \sum_{m' \neq m} d_{m'n\mathbf{k}}(t) \langle \hat{e}_{\mathbf{k}m'}^\dagger \hat{e}_{\mathbf{k}m} \rangle. \end{aligned} \quad (\text{A8})$$

The nonlinear contributions to the above equation include Phase Space Filling (first line), transient changes in the non-equilibrium hole states due to the non-adiabatic magnetic exchange interaction $\Delta H_{exch}(t)$ (second line), and coupling to h - h (third line) and e - e (fourth line) Raman coherences. The coupled Eqs. (A6), (A7), (A8), and (11) describe photoexcitation of non-thermal carriers modified by the local spin rotation. They were derived

in Refs. [3,17] using the Hartree-Fock factorization.^{13,62} To obtain meaningful numerical results, we readjust our basis $\hat{h}_{-\mathbf{k}n}$ to reflect the eigenstates of $H_b(\mathbf{S}_0)$ following large changes in S_0 during 360° switching.

2. Adiabatic/Fermi-Dirac anisotropy

The equilibrium mobile carriers can be described by Fermi-Dirac populations, $f_{n\mathbf{k}}$, of the eigenstates of the adiabatic Hamiltonian $H_b(\mathbf{S}_0)$, which determine the quasi-equilibrium anisotropy field \mathbf{H}_{FS} , Eq. (6).^{25,32,37} We simplify this thermal contribution by neglecting any laser-induced changes in carrier temperature and chemical potential, which add to our predicted effects. A laser-induced thermal field $\Delta \mathbf{H}_{FS}(t)$ develops indirectly from fs spin-orbit torque as the net spin of the hole Fermi sea bath adjusts to the new non-equilibrium direction of $\mathbf{S}(t)$.¹⁷ As already seen from calculations of magnetic anisotropy that assume a Fermi-Dirac distribution,^{6,37} the small ($\sim \mu\text{eV}$) free energy differences with \mathbf{S} result in anisotropy fields of the order of 10's of mT. The discrepancies between theory and experiment seem to imply that non-equilibrium distributions broad in energy are necessary to explain the magnitude of the observed effects.²⁸ Our time-domain calculation of laser-induced magnetic anisotropy driven by photoexcited fs population agrees with experimental measurements. However, we must still include the thermal Fermi sea anisotropy in order to describe the four-state magnetic memory. For this we express the free energy in the experimentally-observed form dictated by symmetry,^{6,39,61} also obtained by expanding the theoretical expression:⁶

$$E_h(\mathbf{S}) = K_c (\hat{S}_x^2 \hat{S}_y^2 + \hat{S}_x^2 \hat{S}_z^2 + \hat{S}_y^2 \hat{S}_z^2) + K_{uz} \hat{S}_z^2 - K_u \hat{S}_x \hat{S}_y, \quad (\text{A9})$$

where $\hat{\mathbf{S}} = \mathbf{S}/S$ is the unit vector that gives the instantaneous magnetization direction. K_c is the cubic anisotropy constant, K_{uz} is the uniaxial constant, which includes *both strain and shape anisotropies*, and K_u describes an in-plane anisotropy due to strain. We used measured anisotropy parameter values³⁹ $K_c = 0.0144 \text{meV}$, $K_u = 0.00252 \text{meV}$, and $K_{uz} = 0.072 \text{meV}$. We thus obtain the thermal anisotropy field

$$\begin{aligned} \gamma_{\mathbf{H}_{FS}} &= -\frac{2K_c}{S} \hat{\mathbf{S}} + \frac{1}{S} (2K_c \hat{S}_x^3 + K_u \hat{S}_y, \\ &2K_c \hat{S}_y^3 + K_u \hat{S}_x, 2K_c \hat{S}_z^3 - 2K_{uz} \hat{S}_z). \end{aligned} \quad (\text{A10})$$

The above expression describes the equilibrium magnetic nonlinearities of the realistic material. By expressing \mathbf{S} in terms of the polar angles ϕ and θ , defined with respect to the crystallographic axes, we obtain the easy axes from the condition $\mathbf{S} \times \mathbf{H}_{FS} = 0$, by solving the equations

$$2K_c \cos^3 \theta - (K_c + K_{uz}) \cos \theta + \frac{BS}{2} = 0 \quad (\text{A11})$$

$$\sin 2\phi = \frac{K_u}{K_c \sin^2 \theta}, \quad (\text{A12})$$

where we added the external magnetic field B along the [001] direction. For $B=0$, $\theta=\pi/2$ and Eq.(A12) gives the in-plane easy axes of Fig. 1(b). For small K_u , these magnetic states X^+ , X^- , Y^+ , and Y^- are tilted from the [100] and [010] crystallographic directions by few degrees inside the plane.^{33,61} As can be seen from Eq.(A11), the B -field along [001] cants the easy axes out of the plane. In this case, $\theta\neq\pi/2$ is a smooth function of B , consistent with the behavior of the static polar Kerr rotation angle $\theta_K(B)$ observed experimentally (see Fig. 3(a)). Eq.(A12) shows that the out-of-plane tilt θ induces a magnetization rotation inside the plane. It gives two different values for ϕ (X and Y easy axes), which can switch due to either B -field sweeping (as seen in the transverse Hall magnetoresistivity, inset of Fig. 3(a)) or laser-induced fs spin-orbit torque (as predicted here).

Appendix B: Band Continuum of Electronic States

The average hole spin $\mathbf{s}_h(t)$, Eq.(3), that triggers the fs magnetization dynamics here has contributions $\mathbf{s}_{\mathbf{k}n}^h(t)$ from an anisotropic continuum of photoexcited non-parabolic band states. At $\hbar\omega_p\sim 1.5\text{eV}$, this continuum also includes disordered-induced states below the bandgap of the pure semiconductor.²⁸ At $\hbar\omega_p\sim 3.1\text{eV}$, photoexcitation of such impurity band/defect states is small, while the almost parallel conduction and valence bands lead to excitation of a wide range of \mathbf{k} states. Integration over the BZ momenta, as in Eq.(3), presents a well-known challenge for calculating magnetic anisotropies and other properties of real materials.⁶⁰ To simplify the problem, one often calculates the quantities of interest at select \mathbf{k} -points and replaces the integral by a weighted sum over these ‘‘special points’’ (special point approximation).⁶⁰ In our previous work,³ we considered eight special \mathbf{k} -points (Λ -point⁷) along $\{111\}$. While this approximation takes into account the general features of the anisotropic states, it misses important details, such as strong band non-parabolicity, density of states, and photoexcited carrier densities. To compare with the photocarrier densities in the experiment and to address issues such as the frequency dependence of the photoexcited spins, we must include continua of band states in our calculation. Here we integrate over the band-momenta along the eight $\{111\}$ symmetry lines by using the ‘‘special lines approximation’’ discussed in Ref. [64]. At $\hbar\omega_p\approx 3.1\text{eV}$, we approximate the three-dimensional momentum integral by a sum of one-dimensional integrals along the eight \mathbf{k} directions

populated by photoexcited carriers. This simple approximation includes the anisotropic, non-parabolic band continua.⁶⁴ At $\hbar\omega_p\approx 1.5\text{eV}$, Fig. 6(b) was obtained by calculating the one-dimensional integrals along all symmetry lines $\{100\}$, $\{010\}$, $\{001\}$, $\{110\}$, $\{101\}$, $\{011\}$, and $\{111\}$ as in Ref. [64].

Following Ref. [64], we first express

$$\begin{aligned} \frac{1}{V} \sum_{\mathbf{k}} \Delta \mathbf{s}_{\mathbf{k}}^h &= \frac{1}{(2\pi)^3} \int_{BZ} \Delta \mathbf{s}_{\mathbf{k}}^h d\mathbf{k} \\ &= \int \frac{d\Omega}{4\pi} \left[\frac{1}{(2\pi)^3} \int_0^{k_{BZ}} 4\pi k^2 dk \Delta \mathbf{s}_{\mathbf{k}}^h \right], \end{aligned} \quad (\text{B1})$$

where k_{BZ} is the BZ boundary and $d\Omega$ is the angular integral. To calculate the above angular-average, we use the special lines approximation⁶⁴

$$\int \frac{d\Omega}{4\pi} \Delta \mathbf{s}_{\mathbf{k}}^h = \sum_{\alpha} w_{\alpha} \Delta \mathbf{s}_{k\alpha}^h, \quad (\text{B2})$$

where α runs over the dominant symmetry directions, k is the wavevector amplitude, and w_{α} are weight factors. For $\hbar\omega_p\sim 3.1\text{eV}$, the dominant contribution comes from the eight $\{111\}$ symmetry directions, so we approximate

$$\frac{1}{V} \sum_{\mathbf{k}} \Delta \mathbf{s}_{\mathbf{k}}^h = \frac{1}{(2\pi)^3} \sum_{\alpha=\{111\}} w_{\alpha} \int_0^{k_{BZ}} 4\pi k^2 \Delta \mathbf{s}_{k\alpha}^h dk \quad (\text{B3})$$

Instead of eight discrete \mathbf{k} -point populations as in Ref. [3], here we consider continuum distributions along the eight one-dimensional \mathbf{k} -lines. While the estimation of optimum weight factors w_{α} is beyond the scope of this paper,⁶⁰ the order of magnitude of the predicted effects is not sensitive to their precise value. We fix $w_{\alpha}=w$ by reproducing the net photohole density n at one experimentally-measured intensity:

$$\begin{aligned} n &= \frac{1}{V} \sum_{\mathbf{k}} \sum_n \Delta \langle \hat{h}_{-\mathbf{k}n}^{\dagger} \hat{h}_{-\mathbf{k}n} \rangle \\ &= \frac{w}{(2\pi)^3} \sum_{\beta=\{111\}} \int_0^{k_{BZ}} 4\pi k^2 \Delta \langle \hat{h}_{k\beta n}^{\dagger} \hat{h}_{k\beta n} \rangle. \end{aligned} \quad (\text{B4})$$

For the results of Fig. 4, the photocarrier density $n\sim 6\times 10^{18}/\text{cm}^3$ for pump fluence $\sim 7\ \mu\text{J}/\text{cm}^2$ gives $w\sim 1/15$. The same order of magnitude of n is obtained, however, for all other reasonable values of w .⁶⁴ We then used this weight factor for all other laser intensities.

¹ T. Li, A. Patz, L. Mouchliadis, J. Yan, T. A. Lograsso, I. E. Perakis and J. Wang, Nature **496**, 69 (2013).

² J. A. de Jong, I. Razdolski, A. M. Kalashnikova, R. V. Pisarev, A. M. Balbashov, A. Kirilyuk, Th. Rasing, and A. V. Kimel, Phys. Rev. Lett. **108**, 157601 (2012).

³ M. D. Kapetanakis, I. E. Perakis, K. J. Wickey, C. Piermarocchi, and J. Wang Phys. Rev. Lett. **103**, 047404 (2009).

⁴ T. Li, A. Patz, P. Lingos, L. Mouchliadis, L. Li, J. Yan, I. E. Perakis, and J. Wang, arXiv:1409.1591 (2014).

- ⁵ C. Chappert, A. Fert and F. Nguyen V. Dau, *Nature Mater.* **6**, 813 (2007).
- ⁶ T. Jungwirth, J. Sinova, J. Mašek, J. Kučera, and A. H. MacDonald, *Rev. Mod. Phys.* **78**, 809 (2006); T. Dietl and H. Ohno, *Rev. Mod. Phys.* **86**, 187 (2014).
- ⁷ K. S. Burch, D. D. Awschalom, and D. N. Basov, *J. Magnetism and Magnetic Materials* **320**, 3207 (2008).
- ⁸ J. Wang, C. Sun, Y. Hashimoto, J. Kono, G. A. Khodaparast, L. Cywinski, L. J. Sham, G. D. Sanders, C. J. Stanton and H. MuneKata, *J. Phys. Condes. Matter* **18**, R501 (2006).
- ⁹ J. G. Checkelsky, J. Ye, Y. Onose, Y. Iwasa, and Y. Tokura, *Nature Physics* **8**, 729 (2012).
- ¹⁰ Y. Fan, P. Upadhyaya, X. Kou, M. Lang, S. Takei, Z. Wang, J. Tang, L. He, L. Chang, M. Montazeri, G. Yu, W. Jiang, T. Nie, R. N. Schwartz, Y. Tserkovnyak and K. L. Wang, *Nature Materials* **13**, 699 (2014).
- ¹¹ E. L. Nagaev, *Phys. Rep.* **346**, 387 (2001).
- ¹² J.-Y. Bigot, M. Vomir and E. Beaurepaire, *Nature Physics* **5**, 515 (2009); U. Bovensiepen, *Nature Physics* **5**, 461 (2010); C. Boeglin, E. Beaurepaire, V. Halté, V. López-Flores, C. Stamm, N. Pontius, H. A. Dürr and J.-Y. Bigot, *Nature* **465**, 458 (2010).
- ¹³ F. Rossi and T. Kuhn, *Rev. Mod. Phys.* **74**, 895 (2002).
- ¹⁴ D. S. Chemla and J. Shah, *Nature* **411**, 549 (2001).
- ¹⁵ S. T. Cundiff and S. Mukamel, *Physics Today* **66**, 44 (2013).
- ¹⁶ V. M. Axt and S. Mukamel, *Rev. Mod. Phys.* **70**, 145 (1998).
- ¹⁷ J. Chovan, E. G. Kavousanaki, and I. E. Perakis, *Phys. Rev. Lett.* **96**, 057402 (2006); J. Chovan and I. E. Perakis, *Phys. Rev. B* **77**, 085321 (2008).
- ¹⁸ W. S. Fann, R. Storz, H. W. K. Tom, and J. Bokor, *Phys. Rev. B* **46**, 13592 (1992).
- ¹⁹ K. H. Ahn, M. J. Graf, S. A. Trugman, J. Demsar, R. D. Averitt, J. L. Sarrao, and A. J. Taylor, *Phys. Rev. B* **69**, 045114 (2004).
- ²⁰ X. Cui, C. Wang, A. Argondizzo, S. Garrett-Roe, B. Gumhalter and H. Petek, *Nature Physics* **10**, 505 (2014).
- ²¹ A. Patz, T. Li, X. Liu, J. K. Furdyna, I. E. Perakis, and J. Wang, *Phys. Rev. B* **91**, 155108 (2015).
- ²² J.H. Mentink, and M. Eckstein, *Phys. Rev. Lett.* **113**, 057201 (2014).
- ²³ D. B. Turner, K. W. Stone, K. Gundogdu, and K. A. Nelson, *Rev. Sci. Instrum.* **82**, 081301 (2011).
- ²⁴ R. R. Ernst, G. Bodenhausen, and A. Wokaun, *Principles of Nuclear Magnetic Resonance in One and Two Dimensions* (Oxford University Press, New York, 1987).
- ²⁵ A. Kirilyuk, A. V. Kimel, and T. Rasing, *Rev. Mod. Phys.* **82**, 2731 (2010).
- ²⁶ P. Němec, E. Rozkotová, N. Tesařová, F. Trojánek, E. De Ranieri, K. Olejník, J. Zemen, V. Novák, M. Cukr, P. Malý, and T. Jungwirth, *Nature Phys.* **8**, 411 (2012).
- ²⁷ E. Beaurepaire, J.-C. Merle, A. Daunois, and J.-Y. Bigot, *Phys. Rev. Lett.* **76**, 4250 (1996).
- ²⁸ L. Cywiński and L. J. Sham, *Phys. Rev. B* **76**, 045205 (2007).
- ²⁹ J. Wang, C. Sun, J. Kono, A. Oiwa, H. MuneKata, L. Cywiński, and L. J. Sham, *Phys. Rev. Lett.* **95**, 167401 (2005); J. Wang, L. Cywiński, C. Sun, J. Kono, H. MuneKata, and L. J. Sham, *Phys. Rev. B* **77**, 235308 (2008).
- ³⁰ C.-H. Lambert, S. Mangin, B. S. D. Ch. D. Varaprasad, Y. K. Takahashi, M. Hehn, M. Cinchetti, G. Malinowski, K. Hono, Y. Fainman, M. Aeschlimann, and E. E. Fullerton, *Science* **345**, 1337 (2014).
- ³¹ I. Radu, K. Vahaplar, C. Stamm, T. Kachel, N. Pontius, H. A. Dürr, T. A. Ostler, J. Barker, R. F. L. Evans, R. W. Chantrell, A. Tsukamoto, A. Itoh, A. Kirilyuk, Th. Rasing and A. V. Kimel, *Nature* **472**, 205 (2011).
- ³² J.-Y. Bigot, M. Vomir, L.H.F. Andrade, E. Beaurepaire, *Chem. Phys.* **318**, 137 (2005).
- ³³ J. Qi, Y. Xu, N. H. Tolk, X. Liu, J. K. Furdyna and I. E. Perakis, *Appl. Phys. Lett.* **91**, 112506 (2007); J. Qi, Y. Xu, A. Steigerwald, X. Liu, J. K. Furdyna, I. E. Perakis, and N. H. Tolk, *Phys. Rev. B* **79**, 085304 (2009).
- ³⁴ Y. Hashimoto and H. MuneKata, *Appl. Phys. Lett.* **93** (2008).
- ³⁵ J. Wang, I. Cotoros, K. M. Dani, X. Liu, J. K. Furdyna, and D. S. Chemla, *Phys. Rev. Lett.* **98**, 217401 (2007).
- ³⁶ J. Wang, I. Cotoros, D. S. Chemla, X. Liu, J. K. Furdyna, J. Chovan and I. E. Perakis, *Appl. Phys. Lett.* **94**, 021101 (2009).
- ³⁷ N. Tesařová, P. Němec, E. Rozkotová, J. Zemen, T. Janda, D. Butkovičová, F. Trojánek, K. Olejník, V. Novák, P. Malý, and T. Jungwirth, *Nature Photonics* **7**, 492 (2013).
- ³⁸ G. V. Astakhov, A. V. Kimel, G. M. Schott, A. A. Tsvetkov, A. Kirilyuk, D. R. Yakovlev, G. Karczewski, W. Ossau, G. Schmidt, L. W. Molenkamp and Th. Rasing, *Appl. Phys. Lett.* **86**, 152506 (2005).
- ³⁹ D. M. Wang, Y. H. Ren, X. Liu, J. K. Furdyna, M. Grimsditch, and R. Merlin, *Phys. Rev. B* **75**, 233308 (2007).
- ⁴⁰ M. D. Kapetanakis and I. E. Perakis, *Phys. Rev. Lett.* **101**, 097201 (2008); *Phys. Rev. B* **78**, 155110 (2008); *Phys. Rev. B* **75**, 140401 (2007); M. D. Kapetanakis, A. Manousaki, and I. E. Perakis, *Phys. Rev. B* **73**, 174424 (2006).
- ⁴¹ C. Thurn, M. Cygorek, V. M. Axt, and T. Kuhn, *Phys. Rev. B* **88**, 161302(R) (2013); *Phys. Rev. B* **87**, 205301 (2013).
- ⁴² D. E. Reiter, T. Kuhn, and V. M. Axt, *Phys. Rev. Lett.* **102**, 177403 (2009).
- ⁴³ Th. Gerrits, H. A. M. van den Berg, J. Hohlfeld, L. Br and Th. Rasing, *Nature* **418**, 509–512 (2002).
- ⁴⁴ H. W. Schumacher, C. Chappert, P. Crozat, R. C. Sousa, P. P. Freitas, J. Miltat, J. Fassbender, and B. Hillebrands, *Phys. Rev. Lett.* **90**, 017201 (2003).
- ⁴⁵ S. Kaka and S. E. Russek, *Appl. Phys. Lett.* **80**, 2958 (2002).
- ⁴⁶ Ettore Carpene, Christian Piovera, Claudia Dallera, Eduardo Mancini, and Ezio Puppini, *Phys. Rev. B* **84**, 134425 (2011).
- ⁴⁷ H. W. Schumacher, C. Chappert, P. Crozat, R. C. Sousa, P. P. Freitas, and M. Bauer, *Appl. Phys Lett.* **80**, 3781 (2002).
- ⁴⁸ M. Porer, U. Leierseder, J.-M. Ménard, H. Dachraoui, L. Mouchliadis, I. E. Perakis, U. Heinzmann, J. Demsar, K. Rossnagel, and R. Huber, *Nature Materials* **13**, 857 (2014).
- ⁴⁹ A. Patz, T. Li, S. Ran, R. M. Fernandes, J. Schmalian, S. L. Budko, P. C. Canfield, I. E. Perakis, and J. Wang, *Nature Commun.* **5**, 3229 (2014).
- ⁵⁰ M. D. Kapetanakis, P. C. Lingos, C. Piermarocchi, J. Wang and I. E. Perakis, *Appl. Phys. Lett.* **99**, 091111 (2011); *J. Opt. Soc. Am. B* **29**, A95 (2012).
- ⁵¹ K. Shen and M. W. Wu, *Phys. Rev. B* **85**, 075206 (2012); M. W. Wu, J. H. Jiang, and M. Q. Weng, *Phys. Rep.* **493**, 61 (2010).
- ⁵² P. Vogl, H. P. Hjalmarson, J. D. Dow, *J. Phys. Chem.*

- Solids **44**, 365 (1983).
- ⁵³ A. Manchon and S. Zhang, Phys. Rev. B **79**, 094422 (2009).
- ⁵⁴ A. Chernyshov, M. Overby, X. Liu, J. K. Furdyna, Y. Lyanda-Geller, and L. P. Rokhinson, Nature Physics **5**, 656 (2009).
- ⁵⁵ L. Berger, Phys. Rev. B **54**, 9353 (1996).
- ⁵⁶ A. Brataas, A. D. Kent, and H. Ohno, Nature Mater. **11**, 372 (2012).
- ⁵⁷ I. E. Perakis and T. V. Shahbazyan, Surface Science Reports **40**, 1 (2000).
- ⁵⁸ M. E. Karadimitriou, E. G. Kavousanaki, K. M. Dani, N. A. Fromer, and I. E. Perakis, J. Phys. Chem. B **115**, 5634 (2011); M. E. Karadimitriou, E. G. Kavousanaki, I. E. Perakis, and K. M. Dani, Phys. Rev. B **82**, 165313 (2010).
- ⁵⁹ T. V. Shahbazyan, I. E. Perakis, and M. E. Raikh Phys. Rev. Lett. **84**, 5896 (2000).
- ⁶⁰ P. E. Blöchl, O. Jepsen, and O. K. Andersen, Phys. Rev. B **49**, 16223 (1994); H. J. Monkhorst and J. D. Pack, Phys. Rev. B **13**, 5188 (1976).
- ⁶¹ U. Welp, V. K. Vlasko-Vlasov, X. Liu, J. K. Furdyna, and T. Wojtowicz Phys. Rev. Lett. **90**, 167206 (2003).
- ⁶² H. Haug and S. W. Koch, Quantum Theory of the Optical and Electronic Properties of Semiconductors, 4th ed. (World Scientific, Singapore, 2004).
- ⁶³ S. Mukamel, Principles of Nonlinear Optical Spectroscopy, Oxford U. Press, New York (1995).
- ⁶⁴ P. Enders, Semicond. Sci. Technol. **11**, 187 (1996).
- ⁶⁵ J. Wang, Ultrafast Magneto-Optical Spectroscopy, in Optical Techniques for Materials Characterization, R. P. Prasankumar and A. J. Toni Taylor (Eds.) (Taylor and Francis, 2010).
- ⁶⁶ L. Guidoni, E. Beaurepaire, and J.-Y. Bigot, Phys. Rev. Lett. **89**, 017401 (2002); J.-Y. Bigot, C. R. Acad. Sci. Paris, t. 2, Serie IV, 1483 (2001).
- ⁶⁷ A. V. Kimel, G. V. Astakhov, A. Kirilyuk, G. M. Schott, G. Karczewski, W. Ossau, G. Schmidt, L. W. Molenkamp, and Th. Rasing, Phys. Rev. Lett. **94**, 227203 (2005); N. Tesařová, T. Ostatnický, V. Novak, K. Olejník, J. Subrt, H. Reichlova, C. T. Ellis, A. Mukherjee, J. Lee, G. M. Sipahi, J. Sinova, J. Hamrle, T. Jungwirth, P. Němec, , J. Cerne, and K. Vyborny, Phys. Rev. B **89**, 085203 (2014).
- ⁶⁸ N. Tesařová, J. Subrt, P. Maly, P. Němec, C. T. Ellis, A. Mukherjee, and J. Cerne, Rev. Sci. Instrum. **83**, 123108 (2012).
- ⁶⁹ P. Brumer and M. Shapiro, Phys. Today **64**, 11 (2011).
- ⁷⁰ T. Papenkort, V. M. Axt, and T. Kuhn, Phys. Rev. B **76**, 224522 (2007); T. Papenkort, T. Kuhn, and V. M. Axt, Phys. Rev. B **78**, 132505 (2008).
- ⁷¹ R. Matsunaga and R. Shimano, Phys. Rev. Lett. **109**, 187002 (2012).
- ⁷² Y. H. Wang, H. Steinberg, P. Jarillo-Herrero, and N. Gedik, Science **342**, 453 (2013).
- ⁷³ Liang Luo, Ioannis Chatzakis, Aaron Patz, and Jigang Wang Phys. Rev. Lett. **114**, 107402 (2015); L. Luo, I. Chatzakis, J. Wang, F. B. P. Niesler, M. Wegener, T. Koschny, and C. M. Soukoulis, Nature Commun. **5**, 3055 (2014); T. Li, L. Luo, M. Hupalo, J. Zhang, M. C. Tringides, J. Schmalian, and J. Wang Phys. Rev. Lett. **108**, 167401 (2012).
- ⁷⁴ L. C. Lew Yan Voon and L. R. Ram-Mohan, Phys. Rev. B **47**, 15500 (1993).
- ⁷⁵ H. Li, X. Liu, Y.-Y. Zhou, J. K. Furdyna, and X. Zhang, arXiv:1501.02083 (2015).